NTNU – Trondheim
Norwegian University of
Science and Technology

Patterning of the Oxide Mask for Nanowire Growth by Dry Etching

Åsmund Stenhaug Ueland

Nanotechnology
Submission date: July 2015
Supervisor: Bjørn-Ove Fimland, IET
Co-supervisor: Dingding Ren, IET

Norwegian University of Science and Technology
Department of Electronics and Telecommunications

NORWEGIAN UNIVERSITY OF SCIENCE AND TECHNOLOGY

Master's Thesis

Patterning of the Oxide Mask for Nanowire Growth by Dry Etching

---

Supervisor:
Bjørn-Ove Fimland
Department of Electronics
and Telecommunications

Author:
Åsmund Stenhaug Ueland
MTNANO

Co-supervisor:
Dingding Ren
Department of Electronics
and Telecommunications

July 7, 2015

Abstract

In this master's thesis it is investigated how inductively coupled plasma reactive-ion etching, in combination with hydrofluoric acid wet etching, can be used to produce consistent and reliable nanoscaled holes with a high aspect ratio and a flat bottom in a silicon dioxide mask covering a silicon substrate. The inductively coupled plasma reactive-ion etching technique is found to be very promising, however, more work need to be put into finding the right electron resist for the process. The resist used in this thesis, 950 PMMA A2, proved to etch away too fast in the dry etching plasma. Using an aluminium hard mask in replacement for the electron resist mask was also investigated. The results were promising, but the aluminium mask should have been kept as thin as possible.

Samandrag

I denne hovudoppgåva blir det undersøkt korleis induktivt kopla plasmareaktivioneetsing, i kombinasjon med flussyrevåtetsing, kan brukast for å produsere konsistente og pålitelege nanoskalerte hol som er relativt djupe i forhald til deira breidde og har ein flat botn i ei silisiumdioksidmaske som dekker eit silisiumsubstrat. Den induktivt kopla plasmareaktivioneetsingsteknikken blei funnen å vere svært lovande, men meir forsking må til for å finne ein god elektronresist til prosessen. Elektronresisten som blei brukt i denne avhandlinga, 950 PMMA A2, viste seg å etse bort altfor raskt i tørretsingsplasmaet. Å bruke ei aluminiumhardmaske som erstatning for elektronresistmaska blei òg undersøkt. Resultata var lovande, men aluminiumhardmaska skulle ha vore laga så tynn som mogleg.

Preface

This master's thesis has been performed at the Norwegian University of Science and Technology (NTNU), in the department of Electronics and Telecommunications (IET). The work has been done as part of Prof. Bjørn-Ove Fimland and Prof. Helge Weman's group, a research group working with the growth and characterization of gallium arsenide nanowires for optoelectronic applications.

I would like to thank both professors, Prof. Bjørn Ove Fimland and Prof. Helge Weman, for providing me with the opportunity to perform this work and participate in the highly specialized and recognized research they are performing. I would also like to thank my co-supervisor, PhD. Candidate Dingding Ren, who has taught me a lot and been very helpful whenever I encountered any problems.

The Research Council of Norway is acknowledged for the support to NTNU NanoLab through the Norwegian Micro- and Nano-Fabrication Facility, NorFab (197411/V30).

Contents

Abstract (English) iii

Samandrag (Norwegian) iii

Preface iv

Table of Contents v

List of Tables vii

List of Figures ix

Abbreviations xi

1 Introduction 1

2 Theory 3
2.1 Plasma-enhanced chemical vapor deposition 3
2.2 Electron beam physical vapor deposition 6
2.3 Electron-beam lithography 8
2.3.1 Electron and resist film interactions 9
2.3.2 EBL parameters 10
2.3.3 Exposure 12
2.4 Wet etching 15
2.5 Inductively coupled plasma reactive-ion etching 15
2.6 Molecular beam epitaxy 19
2.6.1 Reflection high-energy electron diffraction 23
2.7 The vapor-liquid-solid growth mechanism 27
2.7.1 Gold-catalyzed growth 29
2.7.2 Self-catalyzed growth 30
2.7.3 Position controlled NW growth 31
2.8 Characterization by scanning electron microscopy 33

2.9 Atomic force microscopy . . . 34
2.9.1 Operation modes . . . 37
2.9.2 Limits of AFM . . . 39

3 Experimental **41**
3.1 PECVD deposition of SiO_2 layer on the Si substrate . . . 43
3.2 Electron beam physical vapor deposition of Al . . . 43
3.3 Spin coating on PMMA . . . 44
3.4 Patterning of PMMA by EBL . . . 46
3.5 Transferring the PMMA pattern to Al layer by wet etching . . . 49
3.6 Etching SiO_2 layer by anisotropic ICP-RIE with Al as a hard-mask . . . 50
3.6.1 The etching process - step by step . . . 50
3.7 Stripping off the rest of the Al layer by wet etching . . . 52
3.8 Etching the last part of the SiO_2 layer in the pattern of holes with a HF wet etch solution . . . 52
3.9 Growing nanowires in the holes by MBE . . . 54

4 Results and discussion **55**
4.1 Dry etching patterning with electron resist as mask . . . 55
4.2 Dry etching patterning with aluminium as hard mask . . . 59
4.3 Effect of EBL parameters . . . 67
4.4 Effect of ICP-RIE etching . . . 67
4.4.1 Choosing the material to be patterned and the material to be the hard mask . . . 68

5 Conclusion and future work **71**
5.1 Future work . . . 71

6 Appendix **77**
6.1 ICP-RIE dry etching parameters and their functions . . . 77

List of Tables

3.1 ICP-RIE parameters for etching of SiO_2 with PMMA mask 42
3.2 PMMA thickness of nine samples 45
3.3 EBL exposure parameters 46
3.4 Al etch solution ratios and strengths 49
3.5 ICP-RIE etching rates for various parameter combinations 51
3.6 Piranha etch solution ratios and strengths 52

4.1 Etch rates and selectivity of PMMA and SiO_2 56
4.2 ICP-RIE parameter for etching of Si_3N_4 69

List of Figures

2.1 Illustration of the PECVD reaction chamber and deposition of SiO_2 . . . 4
2.2 NTNU NanoLab's PECVD system 6
2.3 Illustration of the concepts of EBPVD 7
2.4 NTNU NanoLab's AJA Sputter and Evaporator 8
2.5 Illustration of a typical EBL set-up 9
2.6 Illustration of the focal point, working distance and depth of field in an EBL set-up 12
2.7 Area exposure mode by EBL 13
2.8 Circular exposure mode by EBL 14
2.9 One-shot exposure mode by EBL 15
2.10 Illustration of the development of a wet etching profile 15
2.11 Illustration of the ICP-RIE chamber and its etching with SF_6 gas 17
2.12 Schematic of the ion angular distribution function 19
2.13 Molecular beam epitaxy system at NTNU 20
2.14 Source materials in the Varian Gen II Modular system at NTNU 20
2.15 Illustration of the MBE kinetic growth processes 22
2.16 MBE growth modes 23
2.17 RHEED construction of the Ewald's sphere 25
2.18 RHEED construction of the Ewald's sphere showing all the specular beams 26
2.19 RHEED patterns of ZB and WZ structures 27
2.20 Ga pathway under MBE growth of NW 28
2.21 Radial growth of NW by diffusing Ga adatoms 29
2.22 Au-catalyzed growth of a NW by MBE 30
2.23 Self-catalyzed growth of a NW by MBE 31
2.24 SEM image of single Ga droplets in holes made by nanoimprint lithography 32
2.25 Unordered vs. ordered NW arrays 32
2.26 Illustration of the scanning electron microscope 34
2.27 Illustration of the configuration of the AFM 35
2.28 Illustration of the AFM detector 37
2.29 Illustration of the different operation modes of the AFM 39
2.30 Illustrations of AFM limitations 40

3.1 Illustration of SiO_2 etching with PMMA as a mask 41
3.2 Illustration of the overall experimental procedures of this master's thesis . 42
3.3 One of NTNU NanoLab's reflectometers 46
3.4 Sample U14 after EBL and development 47
3.5 PMMA patterned holes of $\sim$ 100 nm 48
3.6 NTNU NanoLab's EBL system 48
3.7 Patterned Al thin film layers 50
3.8 Illustration of a thin SiO_2 layer at the bottom of the patterned holes 53
3.9 The desired profile of the pattern of holes after HF wet etching 53
3.10 A NW obtained after the nine major experimental steps 54

4.1 Illustration of the HF etch profile of a previously tried out etching technique 55
4.2 SEM image of the pattern of holes in SiO_2 etched by ICP-RIE with a PMMA mask 57
4.3 AFM image of the pattern of holes in SiO_2 etched by ICP-RIE with a PMMA mask 58
4.4 AFM profile graph of pattern of holes in SiO_2 etched by ICP-RIE with a PMMA mask 59
4.5 SEM image of the pattern of holes transferred from the PMMA mask to the Al hard mask by etching in Al etch solution 60
4.6 Close-up SEM image of the pattern of holes transferred from the PMMA mask to the Al hard mask by etching in Al etch solution 61
4.7 SEM image of the pattern of holes transferred from the Al hard mask to the SiO_2 layer by ICP-RIE 62
4.8 Close-up SEM image of the pattern of holes transferred from the Al hard mask to the SiO_2 layer by ICP-RIE 63
4.9 Close-up tilted SEM image of NWs at sample with increased Al etch time 64
4.10 Undercut of SiO_2 layer because charge build-up bends the ions 65
4.11 Uneven profiles might lead to NWs growing at an angle 65
4.12 Size distribution of the holes on the Al layers 66
4.13 Illustration of the PMMA patterning profile 67
4.14 Etching profile of low pressure chemical vapor deposition (LPCVD) Si_3N_4 68

Abbreviations

1D	One-Dimensional
2D	Two-Dimensional
AC	Alternating Current
AFM	Atomic Force Microscopy
Al	Aluminium
As	Arsenide
Au	Gold (Aurum)
BEP	Beam Equivalent Pressure
BSE	BackScattered Electron
CAR	Continuous Azimuthal Rotation
CCP	Constant Current Power
CVD	Chemical Vapor Deposition
DC	Direct Current
DI	De-Ionized
DOF	Depth Of Field
EBL	Electron Beam Lithography
eV	electron Volt
Ga	Gallium
He	Helium

HF	HydroFluoric acid
IADF	Ion Angular Distribution Function
ICP-RIE	Inductively Coupled Plasma Reactive-Ion Etching
IPA	IsoPropyl Alcohol
LF	Low-Frequency
LN_2	Liquid Nitrogen
LPCVD	Low Pressure Chemical Vapor Deposition
MBE	Molecular Beam Epitaxy
ML	MonoLayer
N2	Nitrogen gas
NW	NanoWire
PECVD	Plasma-Enhanced Chemical Vapor Deposition
PMMA	Poly(Methyl MethAcrylate)
RF	Radio Frequency
RHEED	Reflection High-Energy Electron Diffraction
Sb	Antimony
SCCM	Standard Cubic Centimeters per Minute
SE	Secondary Electron
SEM	Scanning Electron Microscope
Si	Silicon
Ti	Titanium
US	UltraSonic
VLS	Vapor-Liquid-Solid
W	Tungsten (Wolfram)
WF	Write-Field
WD	Working Distance
WZ	WurtZite
ZB	ZincBlende
Å	Ångström

Chapter 1

Introduction

In recent years there has been a substantial increase in solar power and an increased focus on how to make more efficient solar cells. With nanotechnology as an upcoming science field, there has been keen interest in integrating semiconducting nanowires (NWs) with their unique opportunities into the solar cells. Due to the NWs' small dimensions, they can bring certain desired quantum well effects to help increase the NWs' photon absorption efficiency. The same small dimensions are also the reason that NWs might grow on lattice-mismatched substrates during bottom-up growth, such as in the molecular beam epitaxy (MBE) system [2, 3, 4]. In addition to reducing costs, this can also drive the integration of group III-group V NWs with already existing silicon (Si) based technologies.

Controlling the positioning of the NWs is also becoming increasingly important. Positioning is crucial in order to produce reliable and similar arrays of NWs on a large scale. Controlling the positions on which the NWs grow is usually done by either nanoimprint lithography (NIL) or electron beam lithography (EBL). The pattern consists of recurring small-scaled holes in an array. But since the NWs are to be grown with MBE, the resist has to be removed as it would cause carbon contamination in the MBE chamber. Patterns in the resist must therefore be transferred to another inert material. In this study that material is SiO_2, but other materials can also be used, such as Si_3N_4. The transferring of the pattern is done by etching techniques. Earlier the transfer has been tried out with wet etching. This has resulted in very uncontrollable hole sizes and highly isotropic holes (section 4.1).

In this master's thesis the focus is to improve the control of the hole size and make the holes more similar with a narrower size distribution. The goal was to use inductively couple plasma reactive-ion etching (ICP-RIE) as a dry etching technique to produce more anisotropic holes. ICP-RIE can be used to almost only etch in the downward direction, to produce holes with a high aspect ratio ($\frac{\text{Depth}}{\text{Width}}$), and thus help control the size of the holes. However, as our Si substrate has a high etch rate in the dry etching plasma, the SiO_2 layer should not be etched completely through. That will resulted in uneven and irregular Si surfaces at the bottom of the holes. Therefore, the dry etching needed to stop just before

the Si substrate is reached. The rest of the SiO_2 layer that is left on the bottom of the holes could be etched away by isotropic wet etching using hydrofluoric acid (HF). The goal is that HF will etch away the SiO_2, but leave the Si substrate to produce smooth and even bottoms in the holes. As the HF etching is isotropic, it must be kept as short in duration as possible to avoid unnecessary widening of the holes.

Chapter 2

Theory

2.1 Plasma-enhanced chemical vapor deposition

Plasma-enhanced chemical vapor deposition (PECVD) is a process that serves to deposit high-quality, high-performance thin films of metals or dielectric materials from a gas state to a solid state on a substrate at a relatively rapid manner. PECVD is a type of chemical vapor deposition (CVD) that uses plasma to enhance the chemical reaction rates of the precursors [5]. With the use of plasma, the deposition can take place at lower temperatures and also allow for deposition of organic coatings, such as polymers [6]. The substrate is exposed to volatile precursors, which will then react and/or decompose on the substrate surface to create the desired thin films. Volatile byproducts are also often produced. These must be removed by gas flow through the chamber. The plasma is usually created by radio frequency (RF) or direct current (DC) discharge between the two electrodes situated at the top and bottom of the reaction chamber.

The plasma, where a significant fraction of the atoms or molecules are ionized, typically operates at a few millitorr to a few torr. Low-fractional ionization is quite interesting. At low pressure the energy exchange between the electrons and neutral gas, which is in abundance, is very inefficient. Because the electrons are so light, they manage to obtain a high velocity before the RF field switches, while heavier charged atoms and molecules do not. For this reason, the electrons can be maintained at very high equivalent temperatures, while the heavier atom and molecules remain at ambient temperatures. These high-energy electrons may then induce processes that would otherwise be very improbable at low temperatures. These processes are the dissociation of precursor molecules and creation of relatively large quantities of free radicals.

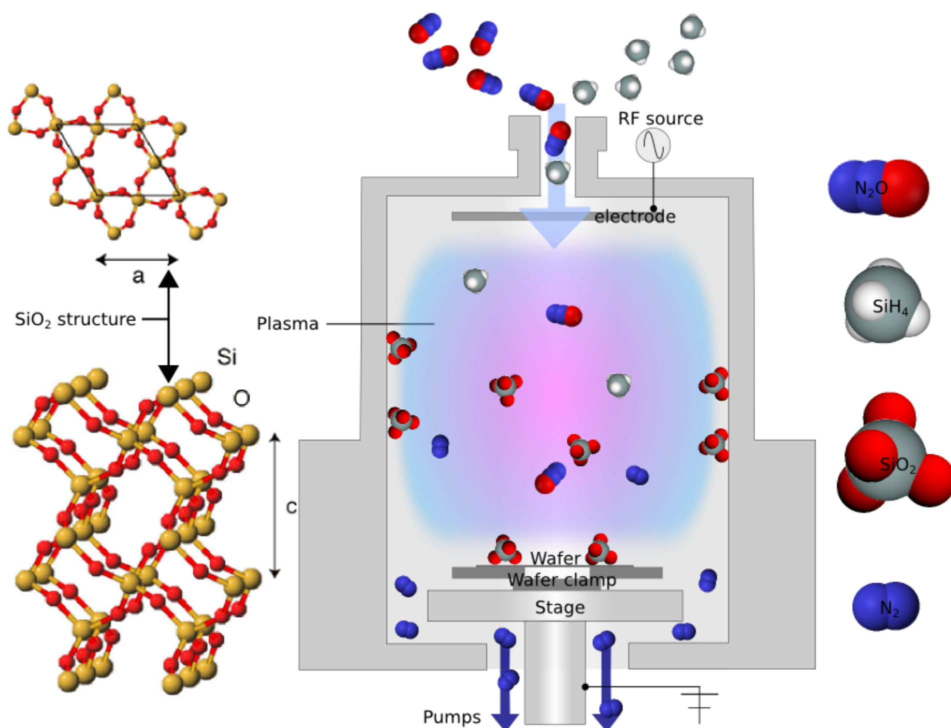

Figure 2.1: Illustration of the PECVD reaction chamber and deposition of SiO_2. This figure shows the main components and concepts of PECVD. The figure includes a gas inlet at the top, an electrode for the AC/RF power, the plasma where the active compounds are made, a stage and a wafer clamp with an attached wafer, where the sample substrate is mounted, and pumps to pump out gas waste products.

Because of the electrons' light weight, the plasma is normally more positive than any object it is in contact with. The reason is that the electrons are highly mobile compared to their positive counterparts, and much more affected by the varying RF field. The difference in voltage typically occurs across a thin sheath region. As ionized species diffuse to the edge of this region, they will feel an electrostatic pull and be accelerated towards the neighboring surface. All surfaces exposed to the plasma will therefore be bombarded by energetic ions. Neutral atom and molecules can diffuse toward the substrate and then condense onto it. The potential across this sheath region is typically 10-20 V, however, the operator is able to tune this potential. This bombardment can increase the thin film density, and help remove contaminants. If desired, it can be combined with high-density plasma to achieve sputtering of the deposited film. The sputtering can help planarize the film and fill holes and trenches.

DC discharge is easily created at a few torr between the electrodes, and is suitable for deposition of conductive materials. When it comes to insulating films, however, they will quickly extinguish this discharge as they are deposited. Normally, a capacitive discharge

is excited by applying alternating current (AC) or RF signal between the electrodes. This configuration is known as a parallel plate reactor. Frequencies ranging between a few tens of Hz to a few thousand Hz will produce time-varying plasmas that are repeatedly initiated and extinguished while frequencies ranging between tens of kilohertz to tens of megahertz result in fairly time-independent discharges. Excitation frequencies in the low-frequency (LF) range ($\sim$ 100 kHz) require several hundred volts to sustain the discharge, while high-frequency plasmas, often excited at the standard 13.56 MHz frequency widely available for industrial use, use much lower voltages. Large voltages lead to high-energy ion bombardment of the surfaces.

The PECVD system at NTNU NanoLab has two power supplies, one RF source (13.56 MHz) and one LF source (50 kHz – 460 kHz) which can be applied to the top electrode one at a time or simultaneously. Sequential use of the two sources allows for stress control of deposited films. The sample stage (bottom electrode) which is grounded is heated to a maximum temperature of 700 C°. Electrons are absorbed at the bottom electrode creating a DC voltage of 10-20 V. In this master's thesis, PECVD is used to deposit SiO_2 thin films. The reaction by which SiO_2 is deposited at NTNU NanoLab's PECVD system is shown in the following chemical equation:

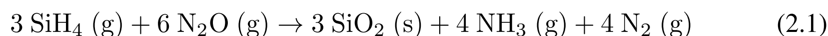

$$3\ \mathrm{SiH_4}\ (g) + 6\ \mathrm{N_2O}\ (g) \rightarrow 3\ \mathrm{SiO_2}\ (s) + 4\ \mathrm{NH_3}\ (g) + 4\ \mathrm{N_2}\ (g) \tag{2.1}$$

Here, silane (SiH_4 (g)) reacts with nitrous oxide (N_2O (g)) to produce the desired silicon dioxide (SiO_2 (s)). The waste products are ammonia (NH_3 (g)) and nitrogen gas (N_2 (g)), which must be pumped out of the chamber.

Figure 2.2: NTNU NanoLab's PECVD system. This instrument can be found in the innermost thin film and dry etch lab finger.

2.2 Electron beam physical vapor deposition

Electron beam physical vapor deposition (EBPVD) can be used to produced a hard mask of aluminium (Al) on top of a SiO_2 layer. This hard mask can then be patterned by EBL (section 2.3) in order to produce a nanoscaled ordered array of holes. EBPVD is a physical vapor deposition technique where a target anode is bombarded with an electron beam given off by a charged tungsten filament under high vacuum. The electron beam causes atoms from the target to evaporate or sublime into a gaseous phase. This gas will then precipitate into solid form when it comes into contact with a solid, thus coating everything in the vacuum chamber that has a direct unobstructed path to the target with a thin layer of the target material. In the EBPVD system, the deposition chamber must obtain a pressure of at least 7.5×10^{-5} Torr in order for the electrons from the electron gun to reach the target material unhindered. However, modern EBPVD systems can utilize an arc suppression system and can be operated at pressure levels as high as 5.0×10^{-3} Torr for situations where it is used in combination with magnetron sputtering [7]. Electron beams can be generated by thermionic emission, field electron emission or the anodic arc method. The generated electrons are accelerated to a high kinetic energy and directed toward the target material by high voltage. When the electrons hit the target material, they will lose their energy very quickly [8]. The electrons' kinetic energy is converted into other forms of energy through interactions with the target material, mostly thermal energy. The thermal energy heats up the target material causing it to melt or sublimate. When the temperature and the vacuum level are sufficiently high, vapor will result from the melted or solid mate-

rial. The resulting vapor can then be used to coat sample surfaces. Accelerating voltages are usually in the range of 3 kV – 40 kV. 85 % of the electrons' kinetic energy can be converted into thermal energy when the accelerating voltage is between 20 kV – 25 kV and the beam current is a few amperes. Some of the incident electrons' energy is lost through formation of X-rays and secondary electron emission.

The sample substrate, on which the film deposition takes place, is fastened to the substrate holder, the substrate holder is attached to the manipulator shaft and the manipulator shaft can move translationally to adjust the distance between the target source and the substrate. The shaft also rotates the substrate at a particular speed so that the thin film will be uniformly deposited on the substrate. A negative bias DC voltage of 200 V – 400 V can be applied to the substrate. In some systems, the substrate can be preheated by focused high-energy electrons from one of the electron guns or by infrared light from heater lamps. This ensures increased adatom-substrate and adatom-film diffusion by providing the adatoms with sufficient energy to overcome kinetic barriers. If a rough film, such as metallic nanorods [9] is desired, one can apply substrate cooling with water or liquid nitrogen to reduce diffusion lifetime, thus positively bolstering surface kinetic barriers. The substrate may also be mounted at a steep angle with respect to the flux to achieve geometric shadowing. This will further enhance the film roughness by ensuring that the incoming line of sight flux only lands on the higher part of the developing film.

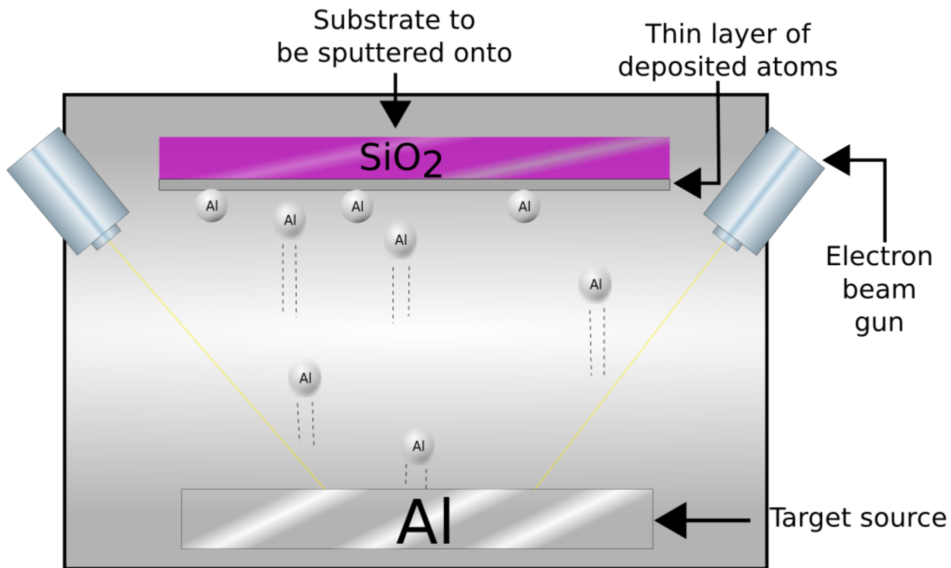

Figure 2.3: Illustration of the concepts of EBPVD. Here one can see electron beam guns heating up the target to a point where Al atoms are released as gas. Because of the low chamber pressure, they will travel in straight lines and deposit on the substrate (and chamber walls *etc*.).

NTNU NanoLab's EBPVD system is an AJA Sputter and Evaporator, model: Custom ATC-2200V. Under operation, it has a chamber pressure of $\sim 10^{-7}$ Torr. A quartz crystal

monitor controls the deposition thickness. The minimum controlled deposition is $\sim$ 1 nm, and the maximum is up to 2 μm. The deposition rate can be varied between 1 $\frac{\text{Å}}{\text{s}}$ and 10$\frac{\text{Å}}{\text{s}}$.

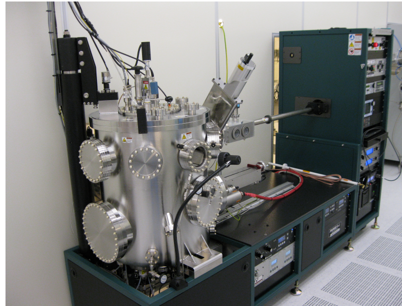

Figure 2.4: NTNU NanoLab's AJA Sputter and Evaporator. This instrument can be found in the innermost thin film and dry etch lab finger.

2.3 Electron-beam lithography

Electron-beam lithography (EBL) is an apparatus were a focused beam of electrons is scanned over a surface, to produced high quality, nano- or micro-sized patterns in the electron-sensitive film to which it is applied. Thus, EBL is quite similar to photolithography, were light is used instead of an electron beam. A high voltage source and a filament are used instead of a light source, and magnetic fields replace the lenses. High vacuum is a requirement, to ensure that the electrons do not collide with anything and scatter before hitting the sample. A typical setup for EBL is shown in figure 2.5. An EBL system is comprised of three main parts: A scanning electron microscope (SEM), a stage and a computer control system. The stage can be controlled with high precision in the x-, y- and z-direction because of a laser-interferometric positioning system with a resolution of 5 nm and a combination of servo-motors and piezo-electric actuators [10]. A computer system is connected to both the SEM and the stage, and it enables detailed control of the beam's shape and position. The computer system is also used to load a pattern and set exposure parameters. The thin film is a chemical solution that covers the substrate that one wants to pattern. The film, called a resist, can either be a positive or a negative resist. A positive resist is a type of resist where the portion of the resist that is exposed to the electron beam becomes soluble to the resist developer. The portion of the positive resist that is unexposed remains insoluble to the resist developer. A negative resist is a type of resist where the portion of the resist that is exposed to the electron beam becomes insoluble to the resist developer. The resist developer will dissolve the unexposed portion of the negative resist. These pattern can subsequently be transferred to the substrate material, often by etching or by deposition.

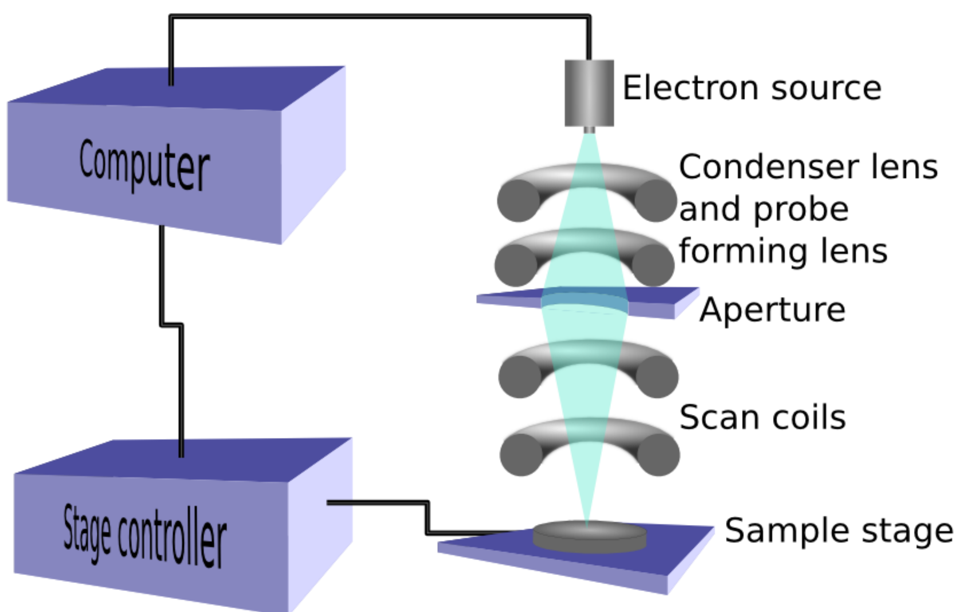

Figure 2.5: Illustration of a typical EBL set-up. This figure shows the main components and concepts of a typical EBL set-up. The figure includes an electron source, an aperture and lenses to control the electron beam, scan coils to steer the electron beam in accordance to the desired pattern, a sample stage, a stage controller and a cumputer.

The primary advantage with EBL is its resolution. Whereas photolithography's resolution is limited by the wavelength of light ($\sim$ 400 nm), resolution of sub-10 nm can be achieved with EBL as the pattern resolution is no longer limited by the wavelength. Another great advantage with the EBL is that it can draw custom made patterns that are easily made on a computer. With the photolithography one must use a physical pattern mask, a disk that lets through light in certain areas. EBL is therefore a very flexible high-resolution technique that works with almost any type of pattern. However, its downside is that it is more time consuming. The electron beam must scan over the entire surface that is going to be exposed, whereas with photolithography, the entire pattern can be exposed with light simultaneously. EBL is therefore often used in nanofabrication research where resolution is more important than throughput.

2.3.1 Electron and resist film interactions

During the exposure of the EBL process, the accelerated beam electrons will interact with the electron-sensitive compounds of the resist. In our studies we have used poly(methyl methacrylate) (PMMA) (IUPAC name: Poly(methyl 2-methylpropenoate)), which is a positive electron resist. The beam electrons will collide with the active compounds in PMMA and break the cross-linking bonds between the molecules and make them shorter and more soluble in the solvent used to develop the patterns. As the accelerated electrons

enter the resist layer they will start colliding and thus scatter. The interaction volume will for this reason be greater than the size of the initial spot of the electron beam. When the initial beam electrons are retarded through the resist, much of their energy dissipation will be picked up by electrons of the molecules in the resist and these will break loose and start colliding themselves as secondary electron with energies ranging between 2-50 eV [11]. These secondary electrons move only a few nanometers before all their energy is transferred in chain scission reactions. These reactions are responsible for the majority of the resist exposure, and due to their spread, they will effectively increase the beam radius by $\sim$ 10 nm. The inelastic collisions cause a slight deflection of the electrons and thus a broader beam as is penetrates deeper into the resist. This is known as forward scatter, as the momentum is mostly conserved in the forward direction. The broadening of the beam as it penetrates the resist is known to be more prominent at lower acceleration voltages. Thin resist layers and higher voltages can be used to minimize this effect.

In addition to the forward scattering, another effect called backscattering may also interfere with the resist. Backscattering exposure, known as the proximity effect, is the result of electrons originating from the beam that pass all the way through the resist layer and are elastically reflected into the resist layer again by interactions with atoms in the substrate. This reentering of the electrons may occur at a considerable distance from the entry point, and may thus interfere with exposure previously done in nearby areas. The energy released from the beam electrons to the electron resist can be modeled as a sum of two Gaussian distributions with different spread values. One spread values for the forwardly scattered electrons, σ_f, and one for the backscattered electrons, σ_b.

$$I_e(r) = \frac{1}{1+\eta}\left(\frac{1}{\pi\sigma_f^2}e^{-\frac{r^2}{\sigma_f^2}} + \frac{\eta}{\pi\sigma_b^2}e^{-\frac{r^2}{\sigma_b^2}}\right) \tag{2.2}$$

Here, $I_e(r)$ is the energy intensity at a distance r from the beam center, σ_f and σ_b are the standard deviations of forward scattering and back scattering respectively, and η is the ratio of backscattered energy to forward scattered energy. At higher acceleration voltages the backscatter distribution becomes wider, and the contribution to exposure becomes lower. This might seem counterintuitive at first, but when the area increases, the relative backscattering per area becomes lower. The effect increases with exposure dose, but can be contained as long as the dose is kept low.

2.3.2 EBL parameters

The EBL system used at NTNU NanoLab is a Hitachi S-4300 Schottky field emission SEM modified with a Raith laser interferometer stage in conjunction with a 6 MHz Raith Quantum pattern generator. In this EBL process there are three main parts of the setup that come together: The design, which contains the patterns that will be written on the sample, the electron beam deflection system, which moves the electron beam according to the pattern using magnetic and electrostatic elements, and the high precision stage, controlled by a combination of servo-motors and piezo-electric actuators.

For a certain magnification in the SEM there is a certain area that can be covered by the

electron beam deflection system with good precision. This area is the write-field (WF), and the appropriate size must be chosen depending on the pattern. The high precision stage allows multiple WFs to be stitched together with less than 20 nm shifts. This makes it possible to put together larger patterns up to 28x28 mm without notable deflection. The beam deflection system is not perfect, however, and it has to be adjusted for each session to ensure it is aligned to the coordinate system of the stage. This adjustment, that should be done at the beginning of each EBL session, is referred to as WF alignment, and it is necessary because the signal-processing chain that controls beam deflection consists of several steps that contribute to long term drift.

There are three considerations that should be kept in mind when the WF size is chosen. First and foremost, the magnification at which the pattern is written will in theory not affect the resolution. This is because only the size of the scanned area changes. The beam does not change. When the magnification is changed, the focusing lenses do not change, and neither does the beam. However, this does not hold up in practice. This is due to the fact that the SEM has two sets of scan coils. One that controls beam deflection at higher magnifications and is more accurate, and one that is active at lower magnifications and deflects the beam with less accuracy. The magnification at which the scanning coils are shifted, depends on the working distance. A click can be heard as they change. Another consideration is pattern distortions. Such distortions can be introduced by operating the scanning coils at the limit of their scan range. If a large area is scanned at low magnification, more current is required by the scan coils to get them to shift the beam toward the outer edges of the scan area. This may result in pattern artifacts. For this reason it is important to always place features to be written close to the center of the WF. Thirdly, one should ensure that the sample is well focused, even if it has height differences. This can be done by adjusting the depth of field (DOF). The distance between the lower part of the objective lens and the substrate surface is known as the working distance (WD), and is set by adjusting the sample stage. The DOF scales linearly with the chosen WD, and also depends on the size of the objective lens aperture (A) and the magnification (M) (see figure 2.6). The DOF can be calculated based on the following relation

$$DOF\,(\mu\mathrm{m}) = \frac{4 \cdot 10^5 \cdot WD\,(\mathrm{mm})}{A\,(\mathrm{mm}) \cdot M} \tag{2.3}$$

Half the distance of the DOF is the distance from the focus plane at which the signals from two pixels overlap enough to cause a blurry image (see figure 2.6). If there are problems with underdeveloping or completely undeveloped areas due to large height differences across the sample, one might solve this by increasing the DOF by increasing the WD.

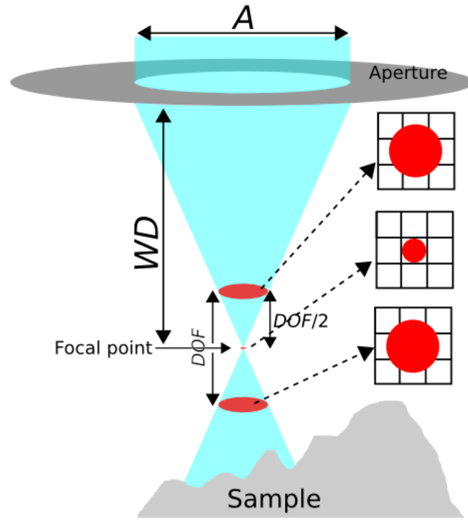

Figure 2.6: Illustration of the focal point, working distance and depth of field in an EBL set-up. This figure shows how the working distance affects the depth of field. When the sample has large height differences, one might need to increase the working distance in order to keep the entire sample in focus (*i.e.* inside the depth of field). $\frac{DOF}{2}$ is the distance at which the diameter of the beam at the surface becomes twice the size of one pixel for the current magnification.

2.3.3 Exposure

To ensure that desired pattern is produced, several exposure parameters must be optimized. Parameters that should be considered are the electron beam current, the beam's dwell time and the step size of the pattern. The exposure dose, D, can be found using the following relation:

$$D = \frac{I \cdot t}{s^2} \tag{2.4}$$

Here, I is the beam current in ampere (A), t is the dwell time in seconds (s) of the beam in each step, and s is the step size i meters (m). The step size is usually set to be equal in the x- and y-direction, and is thus squared. Typical values for the exposure dose are 0-200 $\frac{\mu \mathrm{As}}{\mathrm{cm}^2}$. Normally, one would adjust the desired exposure dose, beam current and step size. Then the EBL machine computes the dwell time.

Exposure mode is also an important parameter of the exposure. It can affect both pattern exposure and exposure time. Exposure time is the total time it takes for the EBL to complete the entire exposure pattern. There are three exposure modes that can be used when the desired pattern is an array of nanoscaled holes. These are area exposure, circular exposure and one-shot exposure. S. Sandell has investigated the time consumption of the different exposure modes in the spring of 2012 at NTNU. Her findings, with regard to time, when exposing a 100 μm $\times$ 100 μm pattern made up of an array of circular dots of $\sim$ 100 nm is given below [12].

- **Area** exposure: 49 min 7 s
- **Circular** exposure: 2 min 40 s
- **One-shot** exposure with 5 ms dwell time: 51 s

Area exposure

In area exposure the beam scans across the sample in the x- and y- direction. A circular feature will be divided into trapezoids, and the beam is blanked when it moves between these trapezoids. Thus, this may lead to rough edges for not straight lines, such as a circle.

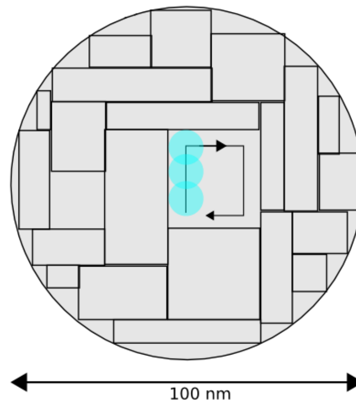

Figure 2.7: Area exposure mode. Here, the pattern of a circle with a diameter of 100 nm is exposed by area exposure mode. For small circles, this is the slowest exposure mode. This is because the pattern is divided into rectangles and trapezoids.

Circular exposure

Circular exposure mode may be used for completely filled and circular features. The beam exposes the sample by writing rings that decrease in size. This reduces the need for moving the stage without doing exposure and is therefore a faster mode for circular shapes than area exposure. The outer edges will also be sharper than with area exposure.

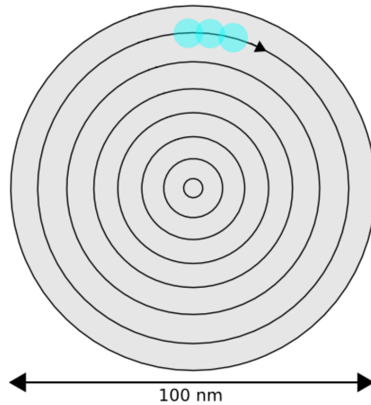

Figure 2.8: Circular exposure mode. Here, the pattern of a circle with a diameter of 100 nm is exposed by circular exposure mode. For small circles, this is the second fastest exposure mode. This is because the patterning is done by writing circles that decrease in size as the exposure goes on. This technique can only be done on circular, completely filled features.

One-shot exposure

One-shot exposure takes advantage of the fact that both the beam and holes in the pattern array have circular shapes. Technically, this is a type of area exposure, but the step size is very large. The step size in one-shot exposure in in the μm range, while in normal area exposure, the step size a few nanometers. The step size in one-shot exposure is also the pitch size of the pattern. Therefore, as the name implies, only one shot of the beam is done at each hole position in the pattern, but each hole has an extended dwell time compared to area exposure. This will create a circle at the beam position due to electron scattering (section 2.3.1). The current, voltage, and duration of the shot (*i.e.* the dwell time) determine the diameter of the hole. Dwell time may vary between a few hundred μs and a few ms. The resulting holes range from $\sim$ 50 nm to a few hundred nm.

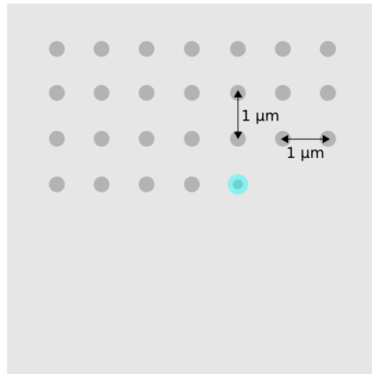

Figure 2.9: One-shot exposure mode. Here, the patterning of an array of small size holes of ~ 100 nm is done by one-shot exposure mode, which is a type of area exposure mode. For circular small holes, this is the fastest way to pattern. This is due to the fact that the pattern and the electron beam share the same shape: They are both circular. Pattering is done by having the beam dwell at a hole position for an extended amount of time. The greater circular shape of the hole is created due to electron scattering.

2.4 Wet etching

Wet etching, or liquid-phase etching, is a chemical etching process where the samples to be etched are immersed in a bath of the etchant. While the etching is ongoing, the solution, or sample, must be stirred around to achieve good process control. This is to ensure contact between the etchant and the material to be etched and hinder waste products in covering the sample surface. Wet etchants are usually isotropic, meaning they will etch equally in all directions. This may result in undercutting of the patterned area (see figure 2.10) and significant changes in device characteristics. Isotropic etching may occur unavoidably, or it may be desirable for process reasons. The liquid etchants are often corrosive in nature.

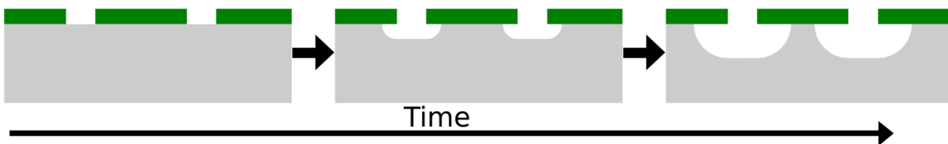

Figure 2.10: Illustration of the development of a wet etching profile. The wet etching technique is usually isotropic in nature, meaning that is preferred etch direction. This often result in an undercut of the patterned area, as seen in this illustration.

2.5 Inductively coupled plasma reactive-ion etching

Inductively coupled plasma reactive-ion etching (ICP-RIE) is a unique dry etching technique where one might get excellent profiles with good anisotropy due to the technique's

high aspect ratio. Aspect ratio is the ratio between the height of the sidewalls compared to the width of the holes. The RIE concept uses low-pressure plasma to generate ion fluxes. These ion fluxes are accelerated toward the substrate due to a DC field bias between the top of the chamber and the bottom where the substrate is situated. The positively charged ions are thus bombarding the substrate, making the etching technique physical, as well as chemical. However, it is a great advantage to be able to separately control the plasma density without affecting the ion energy. This was where the ICP-RIE was introduced. In the inductively coupled plasma RIE, there is a separate plasma generating field, in addition to the DC bias between the top and the bottom of the chamber.

As mentioned, the etching is both chemical and physical. The ICP generator is responsible for making the chemically active ions and radicals. The ICP generator is a conducting coil with an AC flowing through it. The coil is wrapped around the reaction chamber (see figure 2.11) and generates a fluctuating magnetic field. This fluctuating field will in turn induce an electric field that circulates at the top of the chamber. Electrons are accelerated by this electric field and collide with slower moving molecules of the gas or gases that are introduced into the chamber. When the molecules are hit by the fast moving electrons, one or more of their electrons might be knocked off, to ionize the gas or create reactive radicals. When the rate at which ions are made is greater than the rate at which they are lost, the plasma ignites. The glow that can be seen from the plasma comes from the energy released when electrons recombine with ions and are returned to a lower energy state. This energy is very species specific and depends greatly on the gases in the chamber. It can also be used as a good indicator that plasma is satisfactory.

When good plasma is achieved, one would want to guide the positive ions toward the substrate. This is done by having the substrate situated below the glow discharge region, on a capacitively coupled electrode. A generator applies power to this electrode at a frequency of 13.56 MHz. Electrons, which are much lighter than the relatively heavy ions, are able to follow this rapidly changing field. The heavy ions, on the other hand, are all relatively unaffected because they do not manage to build up a momentum in either direction before the field has changed again. The result is that the electrons collide with the electrode, building up a negative charge and establishing a DC field that accelerates positive ions toward the substrate [13]. Physical etching is achieved when the positive ions of the plasma are accelerated by the DC field and collide with the atoms of the substrate. They will then transfer enough momentum for the substrate atoms to detach from the surface. The chemically active radicals that can be formed when ions recombine with electrons do not respond to the DC field. However, they can still etch the substrate, but in a much more isotropic manner.

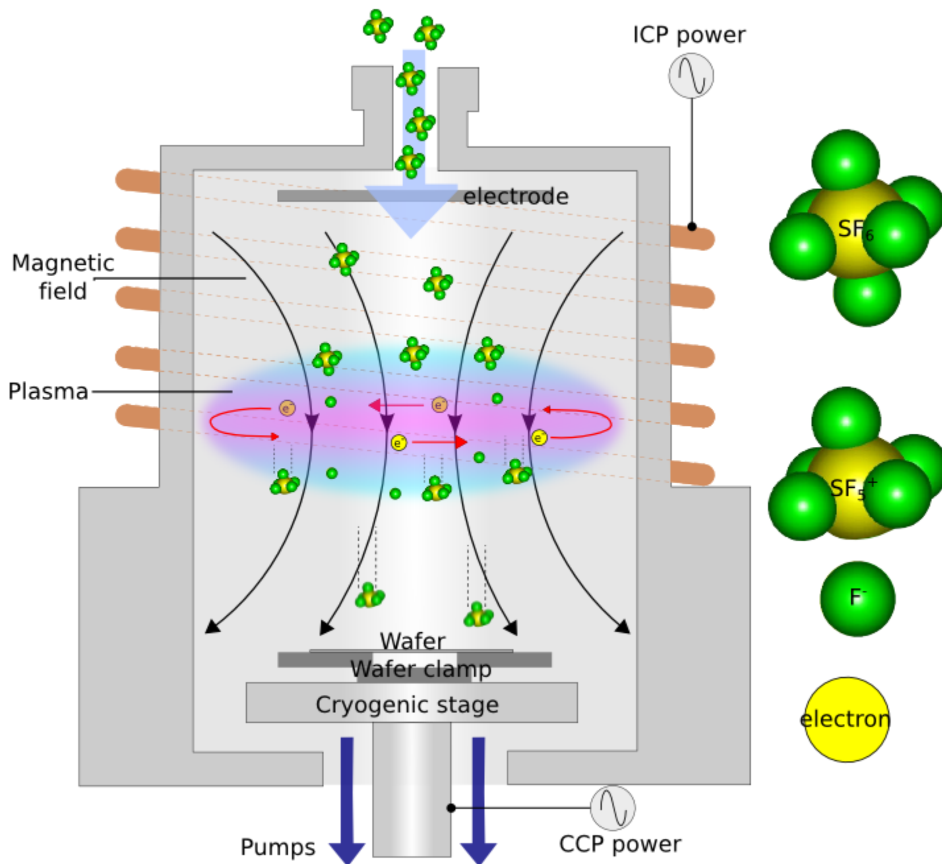

Figure 2.11: Illustration of the ICP-RIE chamber and its etching with SF_6 gas. This figure shows the main components and concepts of the ICP-RIE chamber. The figure includes a gas inlet at the top, electrodes for the CCP, coils wrapped around the chamber for the ICP power (shown in brown), a magnetic field, the plasma with the high-speed swirling electrons, a cryogenic stage, a wafer clamp with an attached wafer, where the sample substrate is mounted, and pumps to pump out waste products.

When it comes to using this technique to do nanoscale etching, one might run into a couple of challenges. First, there is the issue of transport of neutral species in and out of the small-scaled holes. Neutral species that are involved in the etching need to diffuse down into the holes, and etch products need to diffuse out of the holes. As the feature gets smaller it is clear that such circulation will be limited. Circulation will be even more limited as the features become deeper and get a higher aspect ratio as the etching goes on. This may result in a decreased selectivity between the Al hard mask and SiO_2. Another challenge is the risk of charge build-up at the entrances of the holes, as electrons might accumulate the edges of the features. As a consequence, incoming positively charged ions will be deflected toward the sidewalls and increase the lateral etch rate. Also, as ions travel toward the substrate, they will leave the glow discharge region and enter a region known as "dark space", where photon emission due to exited electrons no longer occur. As they enter this region, some of the ions will be scattered by other ions and neutral molecules or atoms. This results in a variety of trajectories that can be characterized by a probability distribution function know as the ion angular distribution function (IADF) (see figure 2.12).

Some common terms used in dry etching literature are selectivity and anisotropy. The term selectivity is used to describe how much faster one type of material is etched away compared to another material. The aim is that a material with low etch rate can be used as a mask for a material with a higher etch rate. The definition of selectivity is

$$S = \frac{\text{Etch rate of material 1}}{\text{Etch rate of material 2}} \tag{2.5}$$

Here, the hard mask material would be material two, with its low etch rate, giving the selectivity a high value. The term anisotropy is used to describe how an etch process prefers to etch in certain directions. For ICP-RIE dry etching the etch direction one would want to look at is the vertical vs. the lateral etch rate. The anisotropy is defined as

$$A = 1 - \frac{\text{Lateral etch rate}}{\text{Vertical etch rate}} \tag{2.6}$$

A good anisotropic etch would thus have a value close to one, as the lateral etch should be close to zero.

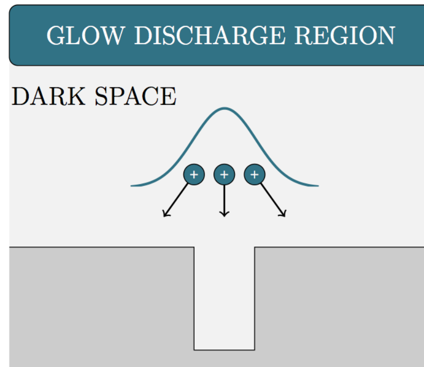

Figure 2.12: Illustration of the IADF. The concept of normal distribution applies to the ion trajectories of e.g. the SF_5^+ ions.

2.6 Molecular beam epitaxy

GaAs and GaAsSb NWs are grown using MBE and the vapor-liquid-solid (VLS) growth mechanism (section 2.7). MBE is an instrument that is used to deposit elements or a mixture of several elements on a surface. In solid-source MBE, elements in ultra-pure form are heated until they slowly evaporate (elements of group III) or sublime (elements of group V and other dopants such as silicon, beryllium and gallium telluride). The gaseous elements will then deposit on the surface in a mixture ratio depending on the flux rates and their individual sticking coefficients. The sticking coefficient is the fraction of the incoming elements that will stick to the surface. The sticking coefficients of group III and dopant elements are normally 1, whereas group V elements have a lower sticking coefficient. This whole process must take place in ultra-high vacuum in order for the atoms to securely hit the wafer surface.

MBE is one of the most versatile and widely used non-equilibrium growth techniques for growing thin, epitaxial films of a wide variety of materials [14]. And it can also be used for growing nanowires when using the right techniques.

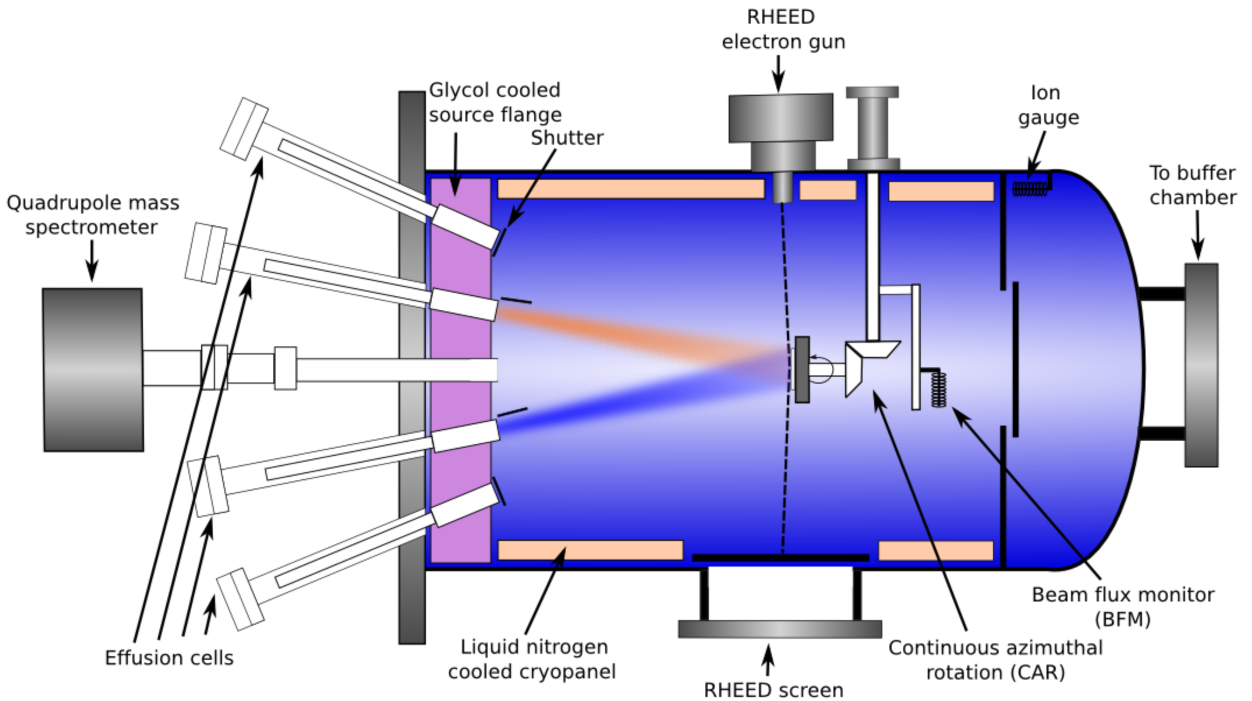

Figure 2.13: Schematic diagram of the MBE system at NTNU used to produce NWs for this master's thesis. This figure shows the main components and concepts of the main chamber in a Molecular Beam Epitaxy system. The figure includes effusion cells, a rotating sample holder, a RHEED gun (section 2.6.1) and screen and cryopanels surrounding in light blue. The effusion cells are heated up resulting in evaporation and sublimation of elements. These elements will then deposit onto the sample when they hit the sample surface, resulting in epitaxial growth.

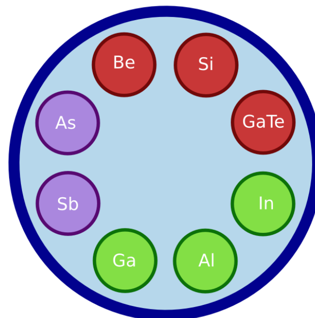

Figure 2.14: Source materials in the Varian Gen II Modular system at NTNU used to produce NWs for this master's thesis. This schematic shows the positioning of the three group III (Ga, Al and In), the two group V (As and Sb) and the three dopants (Be, Si and GaTe) sources.

As can be seen in figure 2.13, the effusion cells in the chamber are all aimed at a small surface. The flux of adatoms coming from an open shutter has to be virtually homogenous over a diameter of at least 3” in front of the substrate. This is to secure an even distribution of adatoms across the whole sample, whose diameter cannot surpass 3” in our MBE system. The ultra-high vacuum in the chamber increases the mean free path of elements departing from the furnaces manifold. This secures that the departing elements will reach the sample surface without colliding with other molecules. The sample surface can be set to rotate to even out the distribution of the elements across the sample. MBE is a quite slow-growing technique, which is often considered to be its main downfall (in addition to being expensive). However, the same slowness can be an advantage at times. Small deposition rates secures that the growth of the structures are mainly governed by the kinetics of the elements and interaction between elements and substrate. Deposition rates as low as 0.1 monolayers (ML) per second can be achieved by controlling the temperatures of the effusion cells [15]. Within the chamber, closing one of the shutters, which are placed in front of the effusion cells, can abruptly halt the flux of elements that have evaporated or sublimed and are moving toward the sample surface. This opens up for the unique possibility to grow heterostructures with abrupt interfaces. In-situ characterization techniques, such as reflection high-energy electron diffraction (RHEED), can be installed inside the chamber and offer unique possibilities to study the composition of the structures while they are being grown.

The growth kinetics of the MBE structures is a result of several dynamic processes taking place simultaneously. In figure 2.15 these processes are illustrated. These processes are deposition, desorption, diffusion, interdiffusion, nucleation, aggregation and downward funneling. All of these kinetic processes, and the scale at which they occur, are strongly dependent on the substrate temperature, the flux ratio of adatoms from group III and group V in the periodic table and their affinity for the substrate and each other and surface reconstructions [15].

There are mainly three growth modes at which the incoming atoms may behave to grow the structures on the sample surface. The birth-and-spread mode is explained by atoms adsorbing to the sample surface. These adatoms will then diffuse around until they bump into another adatom, and they become a pair. These pairs are not likely to break apart again, unless the temperature is sufficiently high. Other adatoms will then adhere to this pair, and thus start the formation of a nucleus. At sufficiently low temperatures, this process will be going on at several sites simultaneously, and the end result is many small island nucleuses spread out across the wafer. When the islands reach a certain number and size, they will efficiently compete for the same incoming atoms and no more islands will be formed. The islands will now grow until the monolayer is completed. At higher temperatures the diffusion length of the adatoms is sufficiently large enough for the adatoms to wander around the entire surface of the wafer. The result is that as soon as one nucleus is formed, the incoming adatoms will be able to reach and adhere to the one nucleus instead of forming new nucleuses. This is called the layer-by-layer growth mode. At lower temperatures and if the monolayer-to-monolayer interaction is sufficiently more favored than the surface-to-

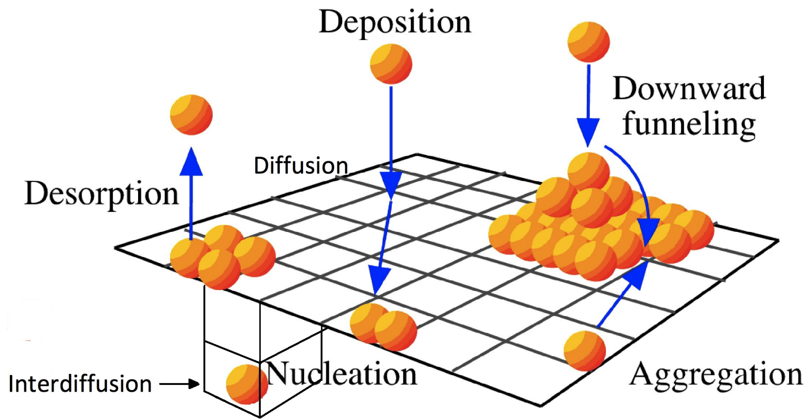

Figure 2.15: Illustration of the MBE kinetic growth processes. The kinetic growth processes of MBE can been seen in this figure. The six processes are deposition, desorption, diffusion, interdiffusion, nucleation, aggregation and downward funneling.

monolayer interaction one can end up with the pyramidal growth mode. This growth mode is governed by the incoming adatoms' preference to bind to other adatoms and avoiding contact with the sample surface. Thus the second and third monolayer of and island will start to be formed long before the first monolayer is completed. The result is small pyramidal structures across the sample surface. See figure 2.16 for an illustration of the different growth modes.

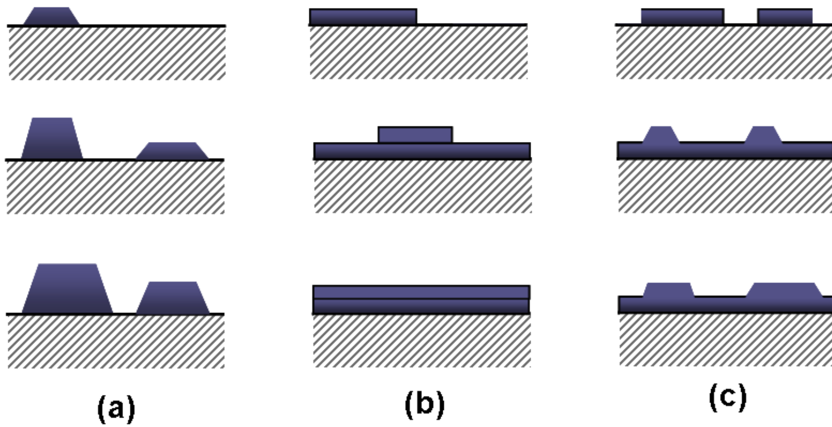

Figure 2.16: Illustration of the three main growth modes that can occur in MBE growth of thin films. This includes **(a)** pyramidal growth mode where interaction between adsorbing adatoms are more favorable than interactions between adatoms and the substrate, **(b)** layer-by-layer mode where interactions between adatoms and the substrate are favorable and the diffusing adatoms have sufficient diffusion length to locate and adhere to a single nucleation site without forming new nucleation sites before the monolayer is completed and **(c)** birth-and-spread mode where interactions between adatoms and the substrate are favorable, but the diffusing adatoms do not have a long diffusion length. The short diffusion length results in several nucleation sites, because the adsorbing adatoms cannot reach the already exsisting ones. After a while enough nucleation sites will have fomed, so that all new adsorbing adatoms can reach one of them and no new ones will be made before the monolayer is complete. The illustration also shows growth over time, as time increases downwards in the figure.

2.6.1 Reflection high-energy electron diffraction

The reflection high-energy electron diffraction (RHEED) system needs an electron source which can emit an electron beam with tunable energy, typically in the range from 8 000 to 30 000 electron volts (eV). Tungsten (W) filaments are the primary electron source for most RHEED systems due to the small work function. The work function is the minimum thermodynamic work (i.e. energy) needed to remove an electron from a solid to a point in the vacuum immediately outside the solid surface. Here "immediately" means that the final electron position is far from the surface on the atomic scale, but still too close to the solid to be influenced by ambient electric fields in the vacuum. The work function is not a characteristic of a bulk material, but rather a property of the surface of the material (depending on crystal face and contamination).

The RHEED setup is also in need of a fluorescent screen inside the MBE chamber, on the opposite side of the electron source (see figure 2.13). The electrons are then drawn from the source by an electric field and aimed at the sample surface at a very low grazing angle ($\theta \leq 2°$). The small grazing angle of the incident electrons allow them to escape the bulk of the sample, get diffracted off the sample and then to reach the fluorescent screen.

The diffracted electrons have constructive interference at certain angles, which are determined by the spacing of the atoms in the sample, the crystal structure of the sample and the wavelength of the incident electron. This wavelength is a function of the applied voltage, given by

$$\lambda = \frac{h}{p} = \frac{h}{m_0 v} = \frac{h}{\sqrt{2m_0 eV}} \tag{2.7}$$

where λ is the de Broglie wavelength (electron wavelength), h is Planck's constant, p is the relativistic momentum, m_0 is the electron mass, v is the electron speed, e is the elementary charge, V is the applied voltage and c is the speed of light. However, when high voltages are applied, the electron's speed will reach values close to the speed of light. When this occurs, relativistic effect must be taken into account in the equation.

$$\lambda = \frac{h}{\sqrt{2m_0 eV}} \overset{\text{r. e.}}{=} \frac{h}{\sqrt{2m_0 eV}} \frac{1}{\sqrt{1 + \frac{eV}{2m_0 c^2}}} \tag{2.8}$$

In the $\overset{\text{r. e.}}{=}$-sign the relativistic effects of the electron reaching speed close to the speed of light is taken into account. Analysis of the diffraction pattern can be used to characterize the crystallography of the sample surface (see figure 2.19).

Since the sample surface is a two-dimensional (2D) crystal surface, it will be represented by a series of infinite lattice rods extending perpendicular to the sample's surface in the reciprocal space [16]. These rods originate at the conventional 2D reciprocal lattice points of the sample surface. One can construct Ewald's spheres when using RHEED to find the crystallographic properties of the sample surface. Ewald's spheres show the allowed diffraction conditions for kinematically scattered electrons in a given RHEED setup. The Ewald's sphere is centered in the reciprocal space around the spot where the electron beam hits the sample surface. The radius of the Ewald's sphere will be equal to the magnitude of the reciprocal of the wavelength of the incident electrons. The reciprocal of the wavelength of the incident electrons is defined as

$$k_0 = \frac{2\pi}{\lambda} \tag{2.9}$$

where k_0 is the incident electron wave vector and λ is the wavelength of incident electrons. Diffraction occurs where the rods of the reciprocal lattice intersect the Ewald's sphere.

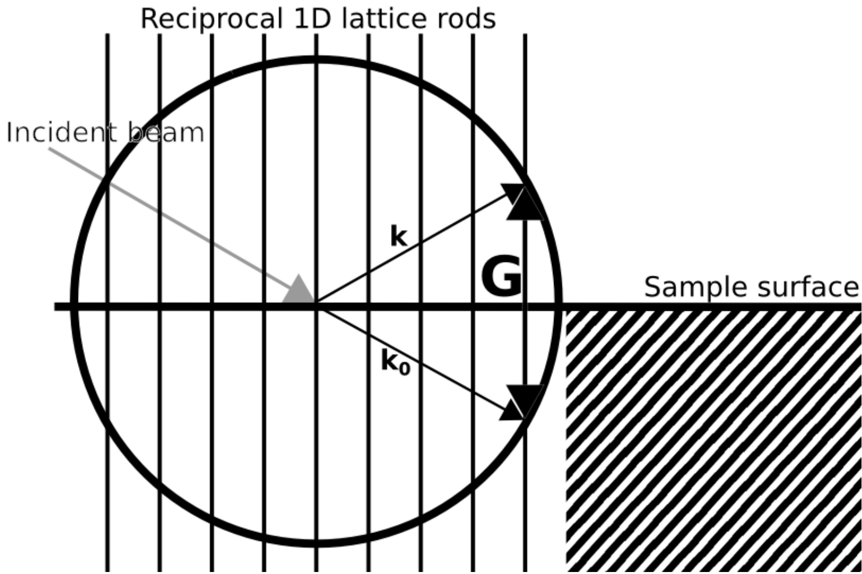

Figure 2.17: The RHEED construction of the Ewald's sphere. Here, one can see the RHEED construction of the Ewald's sphere at the sample surface together with the reciprocal 1D lattice rods of the sample surface. The radius of the Ewald's sphere is equal to the magnitude of the k_0 vector, which is the reciprocal of the wavelength of the incident electrons. The k vector corresponds to an allowed diffraction condition and the G vector is the difference between the k and k_0 vectors. In this figure, the k vector is the specular beam.

The k vectors are electron wave vectors spanning from the center of the Ewald's sphere to any intersection of reciprocal lattice rods with the Ewald's sphere and are labeled such that the k vector that forms the smallest angle with the sample surface is called 0-th order beam. The 0-th order beam is also known as the specular beam. The center of the Ewald's sphere is positioned so that the specular beam forms the same angle with the substrate as the incident electron beam. The specular point has the greatest intensity on a RHEED pattern and is labeled as the (00) point by convention [17]. Figure 2.17 shows a cross sectional view of a single row of reciprocal lattice rods satisfying the diffraction conditions. The RHEED screen shown in figure 2.13 will be located to the right of the reciprocal lattice rods seen in figure 2.17. The RHEED screen will be facing the rods and be perpendicular to the sample surface. The radius of the Ewald's sphere is much larger than the spacing between reciprocal lattice rods because the incident beam has a very short wavelength due to its high-energy electrons. Rows of reciprocal lattice rods actually intersect the Ewald's sphere as an approximate plane because identical rows of parallel reciprocal lattice rods sit directly in front and behind the single row shown in figure 2.17. The vector G defines the reciprocal lattice vector and is the distance between the ends of any two k vectors. Vector G is useful for finding distance between arbitrary planes in the crystal.

$$G = k - k_0 \tag{2.10}$$

The intersections of these effective planes with the Ewald's sphere forms circles, called Laue circles. The RHEED pattern is a collection of points on the perimeters of concentric Laue circles around the center point (see figure 2.18).

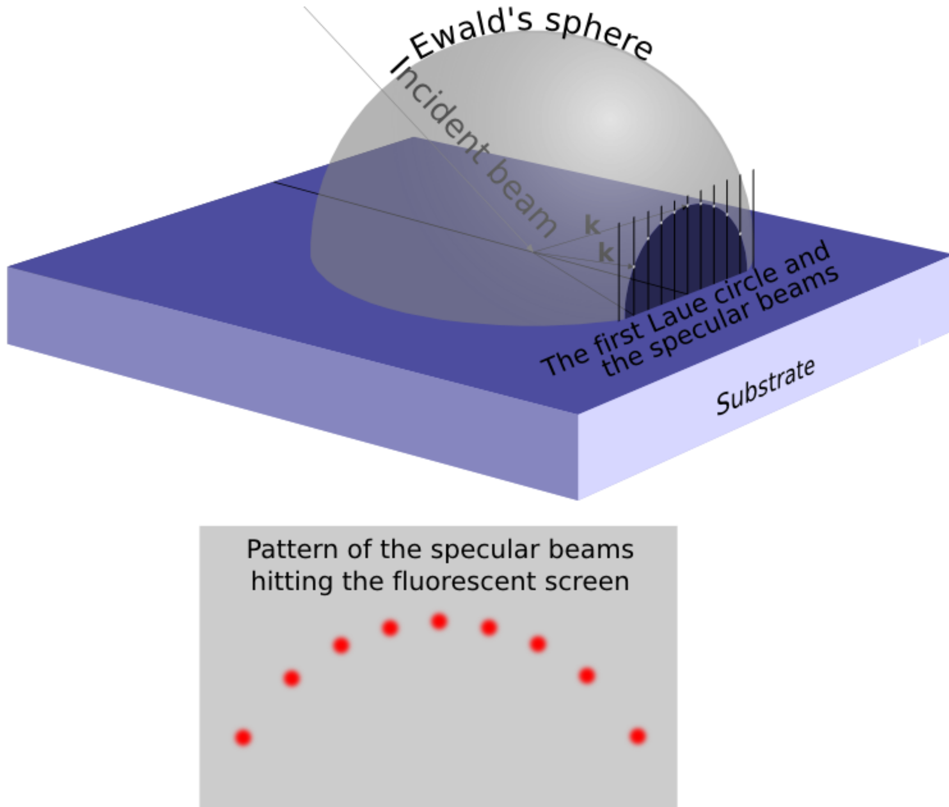

Figure 2.18: RHEED construction of Ewald's Sphere showing all the specular beams. Diffraction forms dots on a semicircle at the intersection of the first reciprocal plane and the Ewald's sphere. Here the specular beams are formed. This semicircle is part of one of the circles formed between the planes of reciprocal lattice rods and the Ewald's sphere. These circles are called Laue circles. The k vectors are all equal in magnitude to the reciprocal of the wavelength of the incident electrons, k_0. Beneath the substrate illustration, one can see the projection of the specular beams onto the fluorescent screen inside the MBE chamber.

Most RHEED systems, e.g. in the MBE system, are equipped with a sample holder that can rotate the crystal around an axis perpendicular to the sample surface. RHEED users rotate the sample to optimize the intensity profiles of the patterns [16].

Since the electrons that hit the sample surface will not all have the same energy, but be spread across a small energy range, the Ewald's sphere will not be infinitely thin. The reciprocal lattice rods will also have a finite thickness, which depends on the quality of the sample surface. Typically terraced structures will have a notable thickness on their rods.

This gives the rods a more plane-like character, leading to the appearance of intensity-modulated streaks on the fluorescent screen.

RHEED can be used in two different modes: Static and dynamic. In static mode the patterns obtained can be used to determine surface re-construction of the material at different conditions. The re-construction is influenced by parameters such as substrate temperature and strain of the epitaxial layer. In dynamic mode one can measure the change in intensity of the central diffraction streak in order to estimate the change in wafer roughness. The wafer roughness will change during the formation of a monolayer by the birth-and-spread mode. The roughness would be low during the start and towards the completion of a monolayer, while it would be high when it is halfway done. Also, the time separation between two adjacent peaks in the RHEED oscillations provides the time it takes for the growth of a single monolayer.

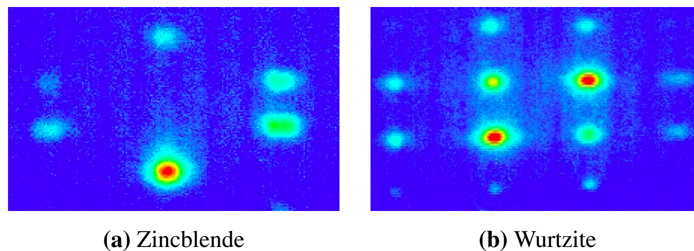

(a) Zincblende **(b)** Wurtzite

Figure 2.19: RHEED patterns of ZB and WZ structures. In (**a**) one can see a RHEED pattern showing the zincblende (ZB) structure in a GaAs NW and in (**b**) one can see a RHEED pattern showing the wurtzite (WZ) structure in a GaAs NW. Since both the Ewald's spheres and the reciprocal lattice rods in both these images have a finite thickness, the spots of the RHEED patterns are stretched out with an intensity-modulated appearance [18].

2.7 The vapor-liquid-solid growth mechanism

The vapor-liquid-solid (VLS) growth mechanism technique that is specifically being used to grow one-dimensional (1D) NW is a bottom-up technique that was first demonstrated by Wagner and Ellis in 1964 [19]. It can be used in different instruments such as chemical vapor deposition (CVD) or MBE. The growth rate of a crystal through direct adsorption of a gas phase onto a solid is very slow. The VLS mechanism speeds up this reaction by the use of a clever catalyst: the liquid droplet. The liquid droplet will easily absorb the vapor to sufficiently high levels (typically a few percent for As) so that the droplet gets supersaturated by the gas species now dissolved in the droplet. The droplet will then reduce its supersaturation by crystallizing out the same species, and thus grow a crystallized solid phase on its underside from nucleated seeds in the liquid-solid interface. The physical characteristics of NWs grown in this manner depend upon size and other physical properties of the liquid droplet. Choosing the liquid alloy and controlling its size can thus control these characteristics.

GaAs NWs grown by MBE was first demonstrated by Wu *et al.* [20] in 2002 and showed that the catalytic activity of the Au droplet to decompose the metallic groups is not the single most important feature for initiating the growth of NWs, as it had been believed until that point. The role of the Au droplet has been related to the chemical potential of Ga adatoms, and how this potential decreases from vapor to the two dimensional (2D) layer, from the 2D layer to the Au-Ga alloy, and lastly from the Au-Ga alloy to the Au-NW interface. Thus, the Au droplet controls the pathway of the Ga adatoms and they will diffuse along the 2D layer (including the NW) to the Au droplet and then precipitate as a part of the NW in a non-reversable manner (see figure 2.20).

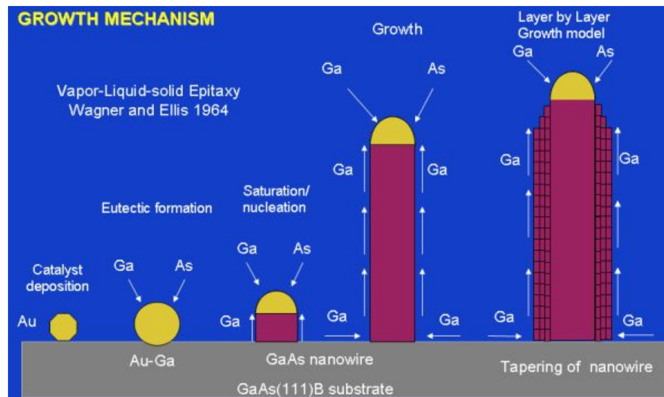

Figure 2.20: Schematic diagram showing the various steps in the VLS growth of a GaAs NW. Here one may clearly see the different pathways the Ga adatoms can use to reach the catalyst droplet: direct impingement to the droplet and surface diffusion from the substrate and the NW to the droplet [21].

As the NW increases in length, some reduction of its diameter is often observed toward the top of the NW. There are two main arguments for this reduction. The first is that as the NW grows, the amount of incoming Ga adatoms to the droplet is reduced due to shadowing from other NWs and that the length of the nanowire surpasses the diffusion length of Ga. When the amount of incoming Ga is reduced the catalyst droplets will shrink and obtain a smaller diameter, resulting in a smaller NW diameter [22]. The second argument is that when less Ga adatoms are able to diffuse the increasing length to the catalyst droplet, this surplus of Ga adatoms will initiate radial growth of the NW by layer-by-layer growth mechanism (see section 2.6) as in figure 2.21. This radial growth only comes into play when the length of the NW exceeds the diffusion length of the Ga adatoms on the NW sidewall [23].

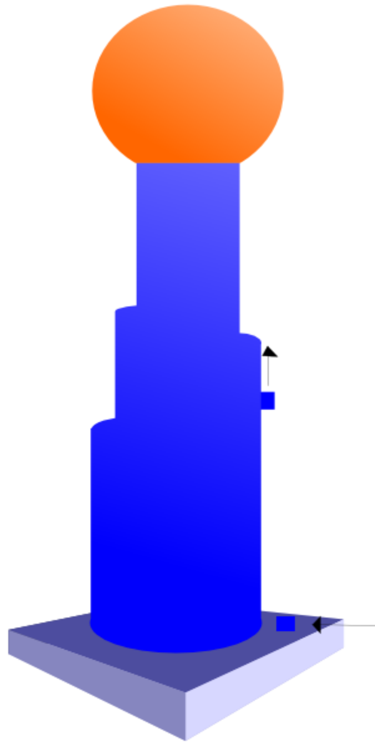

Figure 2.21: Illustration of radial growth of NW by diffusing Ga adatoms. When the NW length exceeds the diffusion length, the droplet size will shrink and excess Ga adatoms can adhere at the base of the NW. The NW in this figure has a length that is longer than the diffusion length of Ga. Therefore one can see Ga adatoms diffusion up the NW, but they will not diffuse all the way to the droplet. This results in a radius build-up near the base of the NW, as can be seen in the figure.

2.7.1 Gold-catalyzed growth

Gold(Au)-catalyzed growth of NWs was much used in almost all material and growth systems some years ago, but is not extensively used today. The formation of the Au droplets is done by depositing a thin film of Au or depositing Au as nanoparticles. When the thin film technique is used, the Au will assemble itself in droplets when the substrate is heated, in order to reduce surface tension energy. The origins for the NWs will be where the droplets form, and growth will take place through the VLS growth mode.

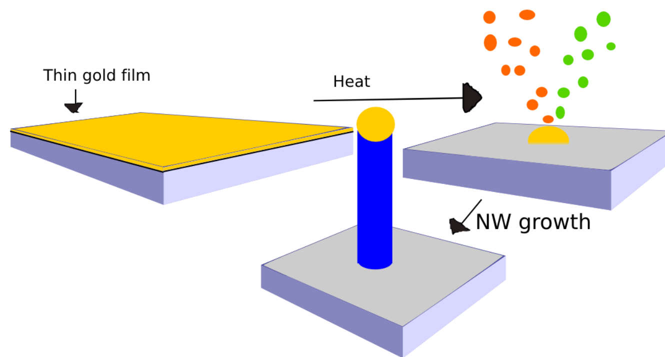

Figure 2.22: Schematic illustration of an Au-catalyzed growth of a NW by MBE. First a thin Au film is deposited. When the substrate is heated up, the film will dewet into Au droplets. These Au droplets will work as catalysts for the VLS growth mode in the MBE chamber.

2.7.2 Self-catalyzed growth

A disadvantage when an Au droplet is used, is that one might introduce tiny fractions of impurities into the nanowires, as some Au might be deposited along with the intended species in the nucleation phase at the liquid-solid interface. There are examples of Au atoms detected in Au-catalyzed growth of NW of silicon (Si) [24], InAs [25] and GaAs [26]. This problem is circumvented when using a group III droplet, so called self-catalyzed growth, as the group III atoms are also used in the NW. One might grow arsenic(As)-limited nanowires when the droplet is made out of Ga, as Ga will then always be in abundance. The formation of the group III droplets is done by first covering the substrate with a native or thin deposited oxide layer that may contain some pinholes. The substrate is then heated to a suitable temperature and group III vapor is supplied. The group III atoms will accumulate in the pinholes, as they do not have a good affinity for the oxide layer. This results in the formation of group III droplets on the substrate. Thereafter the NWs are grown with continuous supply of group III and group V vapors. The vapors absorb into the droplets until supersaturation and then starts to precipitate as solid NW, in a similar manner to Au-catalyzed growth. The self-catalyzed technique was first used by Fontcuberta i Morral *et al.* to grow GaAs NWs using MBE [27].

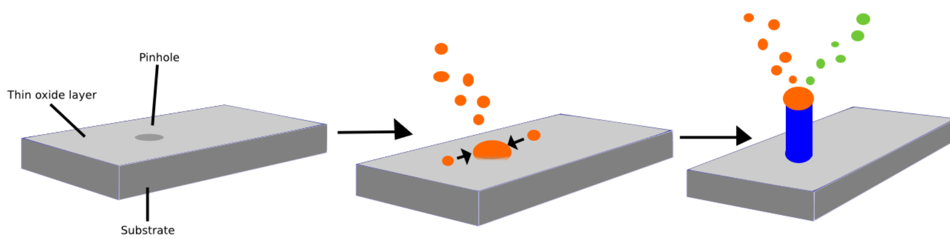

Figure 2.23: Schematic illustration of a self-catalyzed growth of a NW by MBE. A native or thin deposited oxide, to which group III atoms show low affinity, covers the substrate. The oxide contains pinholes where the formation of the group III droplet will occur upon supply of group III vapor from MBE effusion cells. After the droplets are formed, VLS growth continues in a similar manner to the Au-catalyzed growth.

Common for both Au-catalyzed and self-catalyzed growth is that when applying the VLS technique, one must assure that the substrate temperature is above the eutectic temperature of the liquid-alloy droplet particle. This ensures that the droplet stays in its liquid form, upholding its catalytic properties. When the liquid-alloy droplet is supplied with the source material in gas form in a continuous matter, the droplet will absorb a certain fraction of the incoming species. The gas species dissolves in the droplet. After the liquid-alloy droplet is saturated with the maximum gas species it can dissolve, subsequent absorption will result in solid-phase precipitation at the bottom of the droplet [28]. The placement of the catalyst droplet and the group III/group V flux ratio will determine the position and the diameter of the NW. For both of these cases, the position of the droplets will be random, and thus the NWs will grow at random locations and not form regular arrays. This is a problem if the NWs are to be integrated into optoelectric devices.

2.7.3 Position controlled NW growth

The problem with the positioning of the NW can be circumvented by applying nanoimprint lithography (NIL) [29, 30, 31], e-beam lithography (EBL) [32, 33, 34], laser-interference lithography [35] or catalyst droplet deposition through an anodic alumina membrane [20, 36], to predefine the positions of the catalyst droplets. With these techniques it is possible to predetermine the pitch size, array structure and radius of the NWs depending on the patterns or masks that are used with these techniques (see figure 2.24).

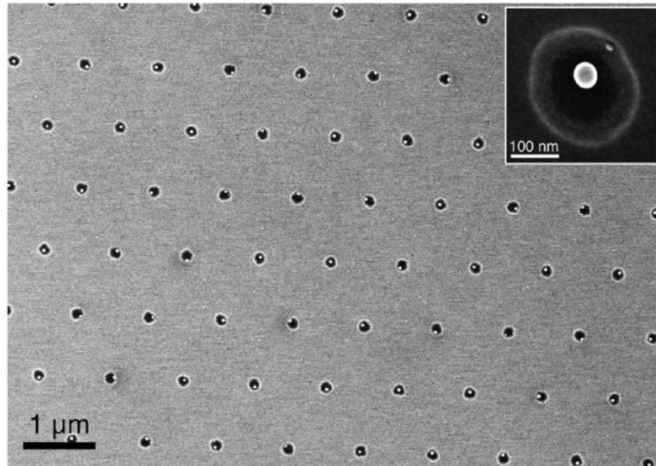

Figure 2.24: SEM image of single Ga droplets in holes made by nanoimprint lithography. Here, one can see the SEM image of single Ga droplets in holes made by NIL on a SiO_2 covered Si substrate formed by pre-depositing Ga for 50 s with a rate of 0.6 ML s^{-1} at a substrate temperature of 630 °C. Inset shows a magnified view of a single Ga droplet in a hole [29].

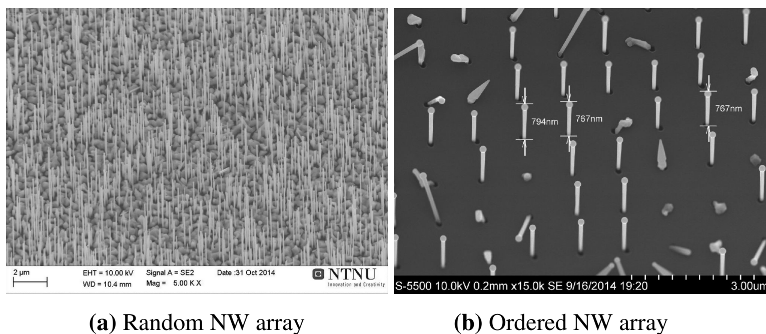

(a) Random NW array **(b)** Ordered NW array

Figure 2.25: Unordered vs. ordered NW arrays. In (**a**) one can see NW growth with uncontrolled positioning due to random pinholes in the native oxide layer where the NWs grow and in (**b**) one can see position-controlled growth of NWs by having the oxide layer patterned with the use of an electron resist, EBL and etching. The pattern that is used makes nanoscaled holes in ordered arrays.

2.8 Characterization by scanning electron microscopy

The scanning electron microscope (SEM) is a type of electron microscope that uses a focused beam of electrons to scan over the sample in a raster scan pattern to produce a sample surface image. Raster scanning means that the focused electron beam scans a thin line along the sample, then it moves back and scans a parallel line just a few nanometers to the side. As this is done over the entire sample, one can get information about the sample's topography and composition. When the electron beam scans the sample, either backscattered electrons (BSEs) or secondary electrons (SEs) can be detected. The electrons in an electron beam of a SEM typically have energies ranging from 100 eV to $30\ 000$ eV, depending on resolution and whether the SEM is in BSE or SE mode. The beam is focused into a point by a few condenser lenses. The point has a diameter of roughly between 0.4 nm and 5 nm. Before the beam hits the sample it also passes through pairs of deflector plates or scanning coils. These are able to bend the beam in x and y direction to obtain the desired raster scan pattern.

BSEs are electrons from the focused electron beam that have been reflected by the sample. These electrons are backscattered or reflected out of the specimen's interaction volume by elastic scattering interactions with the atoms of the specimen. Heavy elements will cause much more backscattering than the light elements because of their high number of electrons that will repel the incoming electrons. Thus, the parts of the sample containing heavy elements will be brighter in the image. BSE detectors are often placed in a ring around the focused electron beam, to pick up backscattered electron regardless of to which side they are being backscattered (see figure 2.26). BSEs can also be used to form an electron backscatter diffraction image, which can be used to determine the crystallographic structure of the specimen.

SEs are low-energy electrons that do not stem from the incident focused electron beam. These electrons are electrons that have been ejected from the k-shell of the atoms of the sample. The k-shell is the innermost electron shell. This ejection is due to inelastic scattering interactions with the beam electrons. Because of their low-energy, these electrons must stem from the top few nanometers of the sample [37]. SEs from deeper within the sample will not be able to escape with their low energy. The SEs are collected by attracting them to a positively biased grid at about $+\ 400$ V, and then further accelerated toward a phosphor or scintillator positively biased to about $+\ 2\ 000$ V. This is done so the electrons will achieve sufficient energy to cause a small flash when they hit the biased scintillator. These signals are then amplified and shown as a 2D image on a video display. The more electrons that reach the detector, the brighter the image will be. If the beam enters the sample perpendicular to the surface, then the activated region is uniform about the axis of the beam and a certain number of electrons will escape from within the sample. As the angle of incidence increases, the "escape" distance of one side of the beam will decrease, and more secondary electrons will be emitted. Thus, steep surfaces and edges tend to be brighter than flat surfaces. This results in images with a well-defined, three-dimensional appearance. When using SEs for imaging the surface of a specimen, one might achieve very good resolution. Image resolution of 0.5 nm is possible with an ultrahigh-resolution scanning electron microscope, as proved by Tanaka *et al.* in 1985 [38].

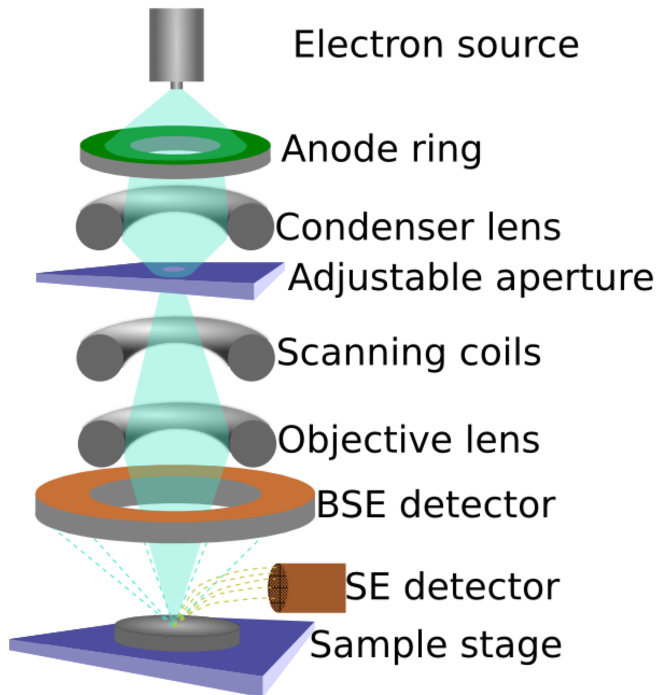

Figure 2.26: Illustration of the concepts and principles of the SEM. In this figure one can see electron gun and the anode ring giving the electron the desired energy. Magnetic lenses focus the electrons into a point. Scanning coils deflect the beam in a desired raster scan patter. The detectors detect BSEs and SEs from the sample.

2.9 Atomic force microscopy

Atomic force microscopy (AFM) is a very high-resolution type of scanning probe microscopy. It has been demonstrated resolution on the order of a fraction of a nanometer. With the AFM it is possible to measure roughness and height variations of a sample surface at a high resolution, to determine mechanical properties of a sample, such as hardness and roughness, and also to perform microfabrication on a sample, such as atomic manupulation. In the scientific field of semiconductor physics, it has been used to identify atoms on a surface, evaluateinteractions between neighboring atoms, and, additionally, measurements of change in physical properties arisen from changing atomic arrangements through atomic manipulation have been made. It is also possible to measure electric potential, when scanning over the sample, if special conducting cantilever are used. In other versions, even electrical conductivity can be measured, by passing small amounts of current through a conducting probe tip [39].

AFM works by having a very sensitive cantilever with a sharp-pointed tip. This tip will then probe the surface of the substrate by being in physical contact with the surface

throughout the measurements. Piezoelectric elements that facilitate tiny, but accurate and precise, movements on command enable this very precise scanning.

The advantages of AFM, when compared to optical microscopy and SEM, are that the AFM has no lenses and no beam irradiation. Therefore, it will not suffer from a limitation in space resolution due to diffraction limits and aberrations. Neither does it need a high vacuum to guide a beam of electrons, nor does it require staining of the sample.

The image formation of the AFM uses color mapping. It correspond some specific value, measured at a certain, very exact location, to each coordinate pair, as the AFM tip scans over the sample. A typical measured variable is height differences. When this function is used, one ends up with a topographic image of the surface of the sample.

The configuration of the AFM (seen in figure 2.27) consists of a cantilever, a sharp tip, a detector, an x-, y-, z-drive, controllers and monitor. The cantilever is a small spring-like structure, that is supported in one end by means of a piezoelectric element. The sharp tip is fixed to the open end of the cantilever, and is used for probing the substrate surface. The detector will detect and monitor the deflection and motion of the cantilever. The x-, y-, z-drive permits the sample stage, and thus the sample, to be displaced in all direction (often based on feedback from the AFM detector). The controllers can be used to produced the right feedback to the drivers when trying to upheld the cantilever at at certain distance from the sample.

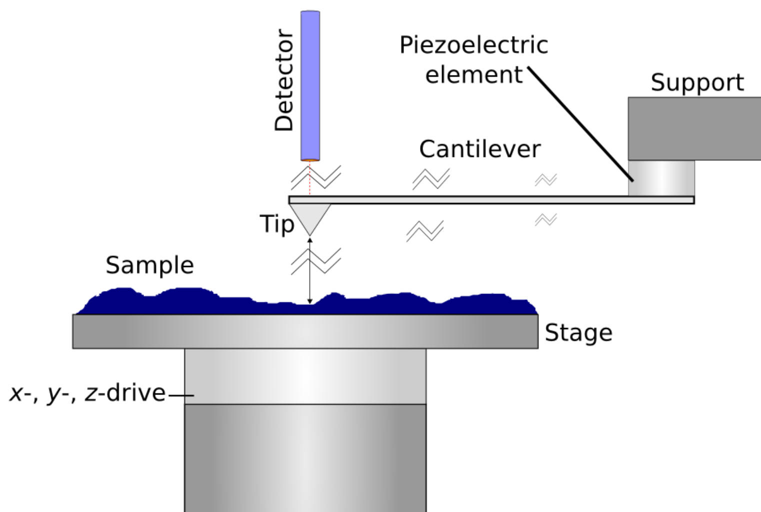

Figure 2.27: Illustration of the configuration of the AFM. This figure shows the configuration and main components of the AFM. The support is there to fix the position of the cantilever, the tip will work as a probe and the piezoelectric element is configured to oscillate the cantilever at its eigenfrequecy.

The cantilever is typically made of silicon or silicon nitride, with a tip radius of curvature on the order of a few nanometers. When the tip is brought into the proximity of the sample surface, forces between the tip and the sample lead to a deflection of the cantilever according to Hooke's law:

$$F(x) = -k \times x \tag{2.11}$$

Depending on the situation, the forces that act upon the tip can be mechanical contact force, van der Waals forces, capillary forces, chemical bonding, electrostatic forces, etc. The deflection of the cantilever is usually measured using a laser spot reflected from the top surface of the cantilever and into an array of photodiodes. Other methods that could be used are optical interferometry, capacitive sensing and piezoresistive AFM cantilevers. However, laser deflection and optical interferometry are thought to be the most sensitive methods. If the tip scans the surface at a constant height, there would be a risk of the tip colliding with the substrate, leading to damage on both tip and substrate. For this reason, in most cases a feedback mechanism is utilized to adjust the tip-to-sample distance at a fixed length to maintain a constant force between the tip and the sample.

Beam deflection measurement

The most widely use method for measuring deflection of the cantilever, is by beam deflection. This method is based on laser light from a solid-state diode being reflected off the back of the cantilever and detected by a very position-sensitive detector consisting of two closely packed photodiodes. These diodes' output is then collected by a differential amplifier. Angular displacement of the cantilever will thus result in one photodiode collecting more light, producing an output signal of the difference between diodes' signal (see figure 2.28). This signal will be proportional to the amount of deflection of the cantilever. This method can detect cantilever deflections of less than 10 nanometer, but it is however limited by thermal noise in its resolution. A long beam path for the deflected beam ensures amplification off the signal.

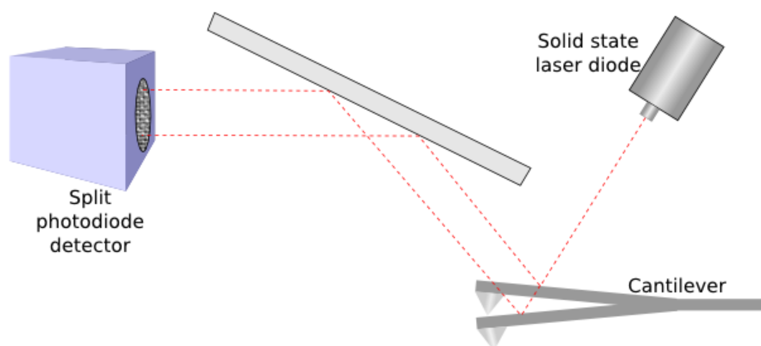

Figure 2.28: Illustration of the AFM detector. This figure shows how a small deflection of the cantilever can produce two quite different beam path. The beam path difference is amplified by a long beam path and mirror. The beam ends up in a spit photodiode detector, which produces an output that results in a topographic image based on the difference in the beam path due to deflection of the cantilever.

2.9.1 Operation modes

The AFM can operate in a variety of modes, depending on the application. Imaging modes and mainly divided into contact mode and dynamic modes. Dynamic modes can be further divided into non-contact mode and tapping mode. In the dynamic modes, the cantilever will oscillate at a given frequency [40].

Contact mode

When using contact mode, the tip is dragged across the sample surface. The surface's contours are thus measured either by using the deflection of the cantilever directly or, more commonly, using feedback signals to retain the tip at a constant distance from the sample surface. The measurements of such a static signal is prone to noise and drift. Low stiffness cantilever are used to amplify the signal by giving more deflection per force. It is important to consider that attractive forces can be quite strong close to the substrate, leading the tip to snap in into the substrate surface. Therefore, contact mode AFM is usually done at a depth where the overall force is repulsive, meaning in firm contact with the solid surface below any adsorbed layers.

Tapping mode

In ambient conditions, sample often develop a liquid meniscus layer. Therefore, keeping the probe tip close enough to the sample for short-range forces to become detectable while preventing the tip from sticking to the surface has been a major problem. Dynamic contact mode was developed to bypass this problem [41]. In this tapping mode, the cantilever is

made to oscillate up and down at or near its resonance frequency. This is done by a small piezoelectric element mounted in the AFM tip holder. The amplitude of this oscillation is relatively large, typically 100 to 200 nm. The interaction of forces acting on the cantilever when the tip comes close to the surface cause the amplitude of this oscillation to decrease as the tip gets closer to the sample. The amplitude change is noticed by the detector and a feedback signal is sent. An electronic servo will use the piezoelectric actuator to control the height of the cantilever above the sample. This is done to maintain a set cantilever oscillation amplitude as the cantilever is scanned over the sample, similar to a set tip-to-substrate distance in contact mode. An image is produced by imaging the force of the intermittent contacts of the tip with the sample surface [42]. The tapping mode lessens the damage done to the surface and the tip compared to the amount done in contact mode. Additionally, there are significant less lateral forces in the tip-sample interaction in tapping mode when comparing to contact mode. Due to its gentle method, tapping mode can even visualize supported lipid bilayers or adsorbed single polymer molecules under a liquid medium.

Non-contact mode

Non-contact mode is a mode where the tip of the cantilever does not contact the sample surface, but instead is oscillated at or near its resonance frequency where the amplitude of the vibrating cantilever is typically a few nanometers down to a few picometers [43]. Long range forces between the tip and the substrate, such as van der Waals forces, act to decrease the resonance frequency. The decrease in frequency is combined with a feedback loop system to maintain a constant oscillation amplitude or frequency by adjusting the average sample-to-tip distance. The height is then measured and plotted to construct a topographical image of the surface of the sample. Since this is a non-contact mode, neither the tip nor the sample will suffer from the same degradation that can be seen with contact mode due to mechanical forces. For this reason, non-contact mode is often the preferred mode for measuring soft samples, like organic thin film or biological samples. In a non-contact mode called frequency modulation, changes in the oscillation frequency will provide information about the sample-tip interaction. Here, frequency can be measured with very high sensitivity and therefore this mode allows for the use of exceedingly stiff cantilevers. Stiff cantilevers provide stability very close to the surface. As a result, the frequency modulation mode was the first AFM technique to provide true atomic resolution in ultra-high vacuum [44].

In another non-contact mode, the amplitude modulation mode, changes in the oscillation amplitude or phase provide the feedback signal for the imaging. In this mode, changes in the phase of the oscillation can be used to discriminate between different types of material on the surface. This technique has been used in the non-contact regime to image with atomic resolution by using very stiff cantilever with small amplitudes and ultra-high vacuum.

Figure 2.29: Illustration of the different operation modes of the AFM. To the left the contact mode can be seen in operation, where the tip is in contact with the substrate during the measuring. In the middle the non-contact mode can be seen in operation, where the tip hovers above the substrate to measure interaction forces during measuring. The the right the tapping mode can be seen in operation, where the tip taps up and down to lessen damage and avoid sticking to the surface.

2.9.2 Limits of AFM

A disadvantage of AFM is its single scan image size. Especially when comparing with the SEM's capability, it becomes evident that it small.The SEM can image an area on the order of square millimeters with a depth of field on the order of millimeters in a single scan, whereas the AFM can only image a maximum height on the order of 10-20 μm and a maximum scanning area of about 150 μm $\times$ 150 μm.

Another limitation is the AFM's scanning speed. The AFM may require several minutes for a typical scan. A SEM is capable of scanning at near real-time. The relatively slow rate of scanning during AFM imaging can often lead to thermal drift in the image, making the AFM less suited for measuring accurate distances between topographical features on the image [45, 46, 47].

Furthermore, there is the possibility of image artifacts, which could be induced by an unsuitable tip, a poor operating environment, or even by the sample itself, as depicted in figure 2.30. These image artifacts are unavoidable, however, their occurrence and effect on results can be reduced through various methods. Artifacts resulting from a very coarse tip can be caused for example by inappropriate handling or collisions with the sample by either scanning too fast or having an unreasonably rough surface, causing substantial wearing of the tip. Due to the nature of AFM probes, they cannot normally measure steep walls or overhangs. Specially made cantilevers and AFMs can be used to modulate the probe sideways as well as up and down (as with dynamic contact and non-contact modes) to measure sidewalls, at the cost of more expensive cantilevers, lower lateral resolution and additional artifacts.

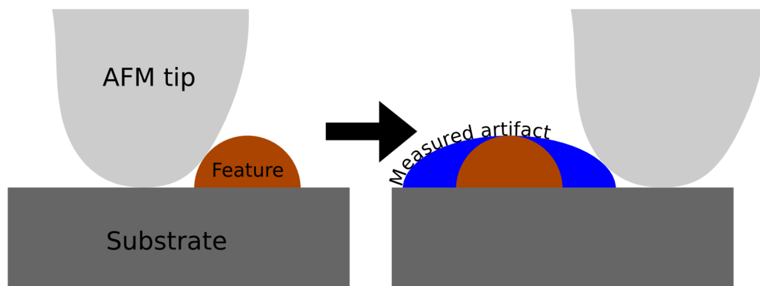

(a) Circle becomes ellipse.

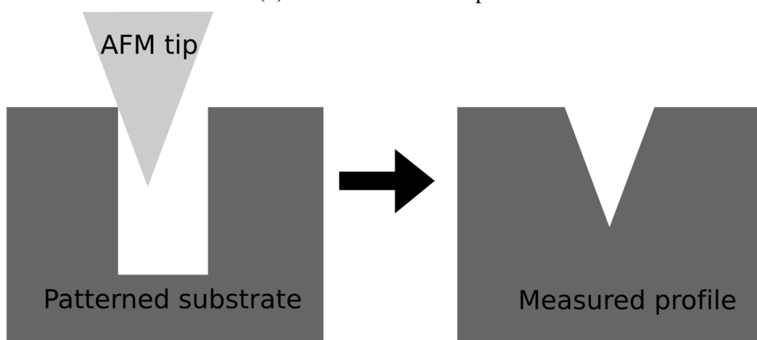

(b) Rectangle becomes triangle.

Figure 2.30: Illustrations of AFM limitations. In (**a**) one can see how a circular feature that is measured with a stump AFM tip becomes an elliptical measured feature in the image. In (**b**) one can see how a sharp high aspect ratio hole become a triangular measured hole even when a sharp tip is used.

Chapter 3

Experimental

Through various experimental procedures, it was sought to find a good way to pattern SiO_2 with nanoscaled, high aspect ratio holes on a Si substrate. One of the methods that were tried out was ICP-RIE dry etching of the SiO_2 with PMMA as a mask (figure 3.1).

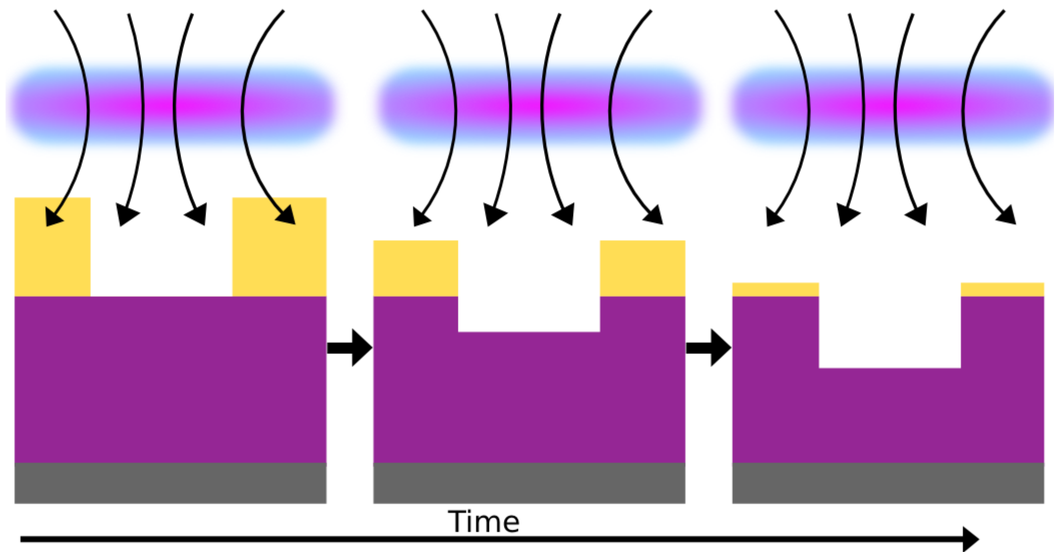

Figure 3.1: Illustration of SiO_2 etching with PMMA as a mask. It was etched with 30 sccm SF_6 gas at -120 °C. The chamber pressure was set to 10 mTorr. ICP power was 1000W, and CCP was 20 W. It was etched for ∼ 20 second, and initial PMMA thickness was found to be 76 nm.

Details of the PMMA spin coating and EBL exposure was the same as for samples U44 and U45 and can be found in sections 3.3 and 3.4. EBL was done with one-shot exposure with 1.0 ms dwell time. The parameters of the ICP-RIE dry etching are given in table 3.1.

Table 3.1: ICP-RIE parameters for etching of SiO_2 with PMMA as the mask. This table shows the ICP-RIE parameters used for this etching procedure (see figure 4.2 for the result).

Etched material	SiO_2
Mask material	950 PMMA A2 - 86 nm thick
Gasses (and flow)	SF_6 (30 sccm)
ICP power	1000 W
RF power	20 W
DC bias	0 V
Temperature	-120 °C
Chamber pressure	10 mTorr
Etch time	20-25 s

Here follow an illustration (figure 3.2) and a list to show the overall procedures and final goal for the experimental work done on the last samples (U44 and U45) in this master's thesis. Through various patterning and etching procedures, the goal is to obtain an ordered array of nanoscaled holes made by anisotropic dry etching on a Si(111) substrate for growth of nanowires with the help of an Al hard mask.

Figure 3.2: Illustration of the overall experimental procedures of this master's thesis. During various procedures and various layers of material, including, Si, SiO_2, Al and PMMA, the goal is to obtain an ordered array of nanoscaled holes of $\sim$ 100 nm, made by anisotropic dry etching on a Si(111) substrate, for growth of nanowires.

The major steps a sample must undergo to obtain this desired structure are:

1. PECVD deposition of SiO_2 layer on the Si(111) substrate.
2. Electron beam physical vapor deposition of Al.
3. Spin coating on PMMA.
4. Patterning of PMMA by EBL.
5. Transferring pattern to Al layer through wet etching.
6. Transferring pattern to underlying SiO_2 layer through anisotropic ICP-RIE etching with Al as a hard-mask.

7. Stripping off the rest of the Al through wet etching.

8. Etching the last part of the SiO_2 layer in the patterned holes, to get through to the Si(111) surface. The is done by wet etching with hydrofluoric acid (HF).

9. Growing nanowires in the holes by MBE.

Now follow sections that address each step in more detail.

3.1 PECVD deposition of SiO_2 layer on the Si substrate

The samples that were used for patterned NW MBE growth in this master's thesis had a 40 nm thick, high-quality thermal SiO_2 layer on top of a Si(111) substrate, bought from an external supplier. The test samples used to study the dry etch rates of SiO_2 were made with NTNU NanoLab's own PECVD machine. The SiO_2 layer grown at NTNU were $\sim$ 300 nm thick and were grown using the following parameters:

- Growth time of 4 minutes.
- Silane (SiH_4 (g)) flow of 8.5 sccm.
- Nitrous oxide (N_2O (g)) flow of 710 sccm.
- Nitrogen gas (N_2 (g)) flow of 161.5 sccm.
- RF forward power of 20 W.
- Capacitor 1 value set to 63.1.
- Capacitor 2 value set to 33.5.
- Table heater set to 300 °C.
- Chiller temperature set to 20 °C.
- Chamber pressure of 1000 mTorr.

3.2 Electron beam physical vapor deposition of Al

A 50 nm thin Al layer was deposited on top of the 40 nm thick thermal SiO_2 layer on top of the Si(111) substrate. The deposition rate was 5 $\frac{\text{Å}}{\text{s}}$. The same deposition rate of 5 $\frac{\text{Å}}{\text{s}}$ was used for the deposition of Ti and Au at sample U14 (figure 3.5).

3.3 Spin coating on PMMA

Before the spin coating was done, I had to make sure the samples were clean. This is done by washing the samples in acetone, followed by isopropyl alcohol (IPA) and de-ionized (DI) water. Then the samples were subsequently dried by nitrogen gas (N2) and plasma ashed using oxygen plasma at 50 % O_2 pressure and power of 50 W for 12 seconds. After these processes the samples were pre-baked for 5 minutes at a hot plate of 180 °C before they were spin coated with PMMA.

Then spin coating was done using 950 PMMA A2. The "950"-prefix means that the solution contains resins of molecular weight of 950'000 u in anisole. The "A2"-suffix show the percentage of anisole in the solution. A higher percentage of anisole make the solution more viscous. The PMMA A2 is thus not a very viscous solution. All the spin coatings were done at 4000 rotation per minute (rpm) for 120 second with a ramp up speed/acceleration of 1000 rotations per minute per second. Thus, four out of the 120 seconds were used to achieve the desired rotation velocity. After the spinning was done, the samples were soft-baked for 10 minutes at 180 °C to make the ready for EBL exposure. Table 3.2 shows various samples of $\sim$ 300 nm SiO_2 on Si(100) that were spin coated and their achieved PMMA thickness. The thicknesses were measured using a specific reflectometer found in NTNU NanoLab (figure 3.3).

Table 3.2: 950 PMMA A2 thin film thickness of samples U8-U15 and U23. Then PMMA was spin coated on samples of ~ 300 nm SiO_2 on Si(100), and measured by a F20 Filmetrics reflectometer.

Sample ID	**Spin speed**	**Spin time**	**Accelaration**	**PMMA thickness**
U8	4000 rpm	120 s	1000 rpm/s	84 nm
U9	4000 rpm	120 s	1000 rpm/s	83 nm
U10	4000 rpm	120 s	1000 rpm/s	86 nm
U11	4000 rpm	120 s	1000 rpm/s	87 nm
U12	4000 rpm	120 s	1000 rpm/s	85 nm
U13	4000 rpm	120 s	1000 rpm/s	86 nm
U14	4000 rpm	120 s	1000 rpm/s	86 nm
U15	4000 rpm	120 s	1000 rpm/s	85 nm
U23	4000 rpm	120 s	1000 rpm/s	86 nm

The mean value of the thicknesses, $\bar{d}$, was found to be

$$\bar{d} = \frac{1}{n}\sum_{i=1}^{n} d_i = \frac{1}{9}\sum_{i=1}^{9} d_i = 85.3 \text{ nm} \tag{3.1}$$

where d_i are the thicknesses listed in table 3.2. The standard deviation of the thicknesses was found to be

$$s = \sqrt{\frac{1}{n-1}\sum_{i=1}^{n}\left(d_i - \bar{d}\right)^2} = \sqrt{\frac{1}{8}\sum_{i=1}^{9}\left(d_i - 85.3 \text{ nm}\right)^2} = 1.22 \text{ nm} \tag{3.2}$$

Figure 3.3: One of NTNU NanoLab's reflectometers. This instrument can be found in the second innermost lithography and wet etch lab finger. This is an F20 model by Filmetrics.

As one can see, the thickness is fairly consistent around 85 nm.

3.4 Patterning of PMMA by EBL

After the spin coating process, the samples were ready to be patterned by EBL. Most of the samples were patterned by the one-shot exposure mode, however, some were also patterned by area exposure mode. Table 3.3 shows the different parameters that were used during the various exposures.

Table 3.3: The EBL exposure parameters. The top four are done with one-shot exposure mode, while the bottom one is done with area exposure mode.

Current	Step size (x and y)	Dwell time	Exposure dose
40 pA	1 μm	0.5 ms	2.0 $\frac{\mu \text{As}}{\text{cm}^2}$
40 pA	1 μm	0.75 ms	3.0 $\frac{\mu \text{As}}{\text{cm}^2}$
40 pA	1 μm	1.0 ms	4.0 $\frac{\mu \text{As}}{\text{cm}^2}$
40 pA	1 μm	1.5 ms	6.0 $\frac{\mu \text{As}}{\text{cm}^2}$
40 pA	4 nm	720 ns	180 $\frac{\mu \text{As}}{\text{cm}^2}$

After exposure, the samples were developed in a mixture IPA and DI water in a 9:1 ratio for 35-60 seconds. Since the PMMA resist is a positive resist, the parts of the pattern that are exposed, will dissolve in this mixture.

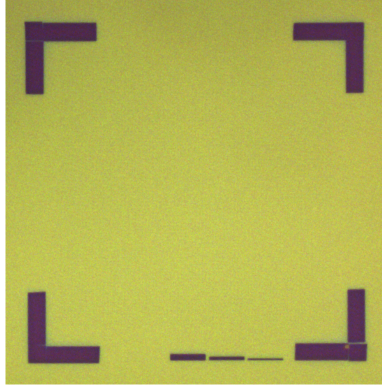

Figure 3.4: Sample U14 after EBL and development. This pattern was made by one-shot exposure with 1.0 ms dwell time and developed for 40 seconds. It is easy to see the characteristic purple color of SiO_2 where the pattern has been developed.

The size of the holes in the PMMA resist have been measured by depositing a 10 nm thick layer of titanium (Ti) followed by a 5 nm thick layer of gold through sputter deposition onto a sample consisting of a $\sim$ 300 nm thick layer of SiO_2 on top of Si(100) that was patterned with PMMA. After sputter deposition the resist was removed with a 5 hours long acetone bath. The result can be seen in figure 3.5.

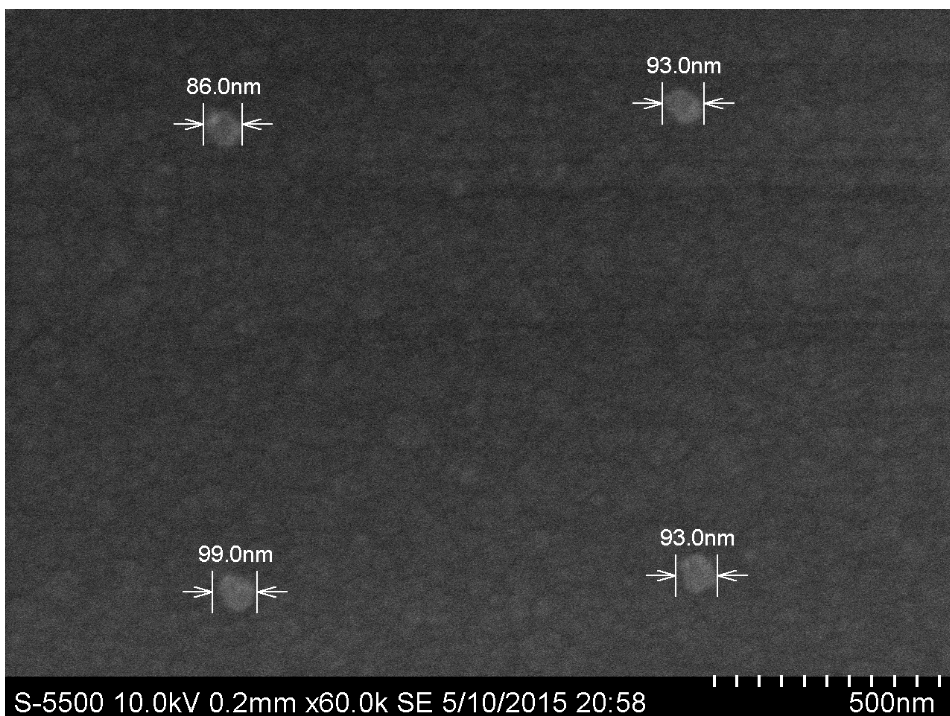

Figure 3.5: PMMA patterned holes of ∼ 100 nm. In this image one can observe the size of the patterned PMMA holes. The patterned PMMA was coated with 10 nm Ti and 5 nm Au by EBPVD and the the resist was stripped off. The size of the Ti/Au islands will indicate the size of the holes at their thinnest, which is at the bottom of the PMMA layer. The holes were made by one-shot exposure with dwell time of 0.75 ms.

Figure 3.6: NTNU NanoLab's EBL system. This is a Hitachi 4300 SEM with Raith laser stage model. This instrument can be found in the second innermost lithography and wet etch lab finger.

3.5 Transferring the PMMA pattern to Al layer by wet etching

In order to transfer the pattern of the PMMA layer onto the underlaying Al layer, we need a good isotropic etchant to etch holes in the Al layer. Several solutions were tested, however, one stood out with a much better result and consistency then the others. It was a mixture of phosphoric acid (H_3PO_4), DI water (H_2O), nitric acid (HNO_3) and acetic acid (CH_3COOH). The mixture ratios and strength of the various compounds and the final solution are given in table 3.4.

The Al etch rate of this solution was tested twice on two samples that were covered with a 50 nm thick Al layer. The times needed to etch through the layers were 28 and 33 seconds, which gives an etch rate of approximately 1.65 $\frac{\mathrm{nm}}{\mathrm{s}}$. This rate is subsequently used when calculating desired etch time of various samples. When etching the Al layer through the PMMA holes, the etch time was generally increased to 150 % because the etch rate is slower in the bottom of a high aspect ratio hole. Sometimes it was even increased to 200 %. Examples are shown in figure 3.7.

Table 3.4: Al etch solution ratios and strengths. This table show the compound, ratios, initial strength of compound and strength of compounds in the finished solution for the best Al etch solution that was tested.

Compound formula	Mixture ratio	Vol% of compound	Vol% of final solution	My mixture volumes
H_3PO_4	26.1	85 vol%	73.0 vol%	172 mL
H_2O	1.82	100 vol%	20.6 vol%	12 mL
HNO_3	1.45	65 vol%	3.12 vol%	9.6 mL
CH_3COOH	1.00	100 vol%	3.30 vol%	6.6 mL

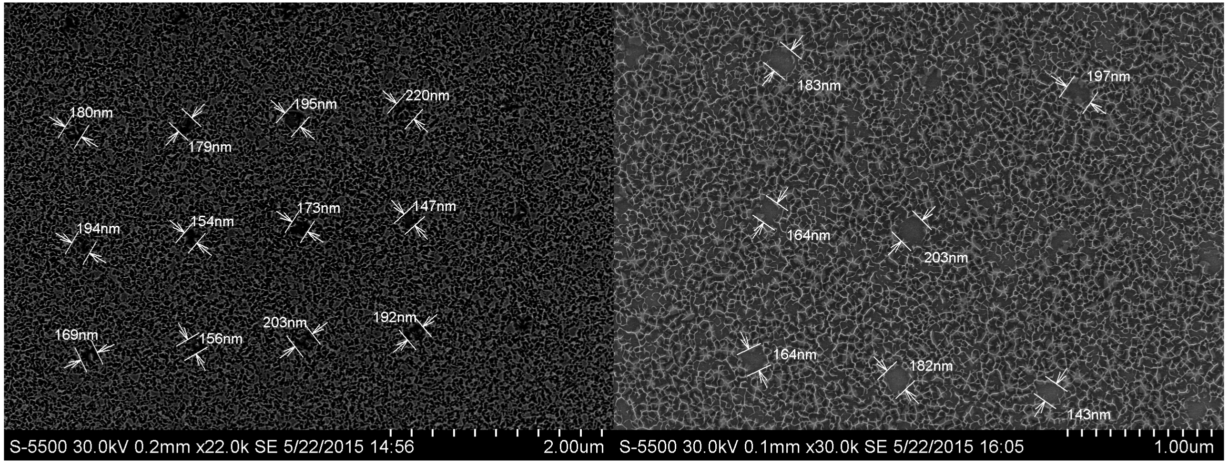

(a) Sample U44 with 150 % etch time **(b)** Sample U45 with 200 % etch time

Figure 3.7: Patterned Al thin film layers. In (**a**) one can see sample U44, that is EBL patterned with one-shot exposure with 1.0 ms dwell time. The pattern has been transferred to the Al thin film, by etching in the Al etch solution (table 3.4) for 45 seconds and the resist has then been removed. In (**b**) one can see sample U45, that is EBL patterned with one-shot exposure with 0.5 ms dwell time. The pattern has been transferred to the Al thin film, by etching in the Al etch solution for 60 seconds and the resist has then been removed.

3.6 Etching SiO_2 layer by anisotropic ICP-RIE with Al as a hard-mask

After the pattern had been transferred to the Al hard mask, the PMMA layer was removed in an acetone bath. It was then washed with IPA and DI water and dried with N2. The sample is then attached to a 4” Si carrier wafer using a thin layer of Fomblin vacuum oil. The oil ensures good thermal contact and heat dissipation and proper cooling of the sample. No oil should be exposed, as this will contaminate the chamber during the etch process. The carrier is then loaded into the chamber, and the etch recipe is started.

3.6.1 The etching process - step by step

The following steps list and arrange all the necessary procedures of the ICP-RIE etching. Are more extensive and complementary list, which also describes the function of the steps, can be found in section 6.1 in the appendix.

1. When the sample has been loaded into the reaction chamber, helium (He) flows against the backside of the sample carrier to achieve a set pressure of 10 Torr. The He is continuously cooled by liquid nitrogen (LN_2).

2. Since our process will take place at -120 °C, the next step is usually cooling of the stage (unless the intrument has just been used at this temperature, and is already at -

Table 3.5: ICP-RIE etching rates for various parameter combinations. This table show the various etching parameter and their obtained etch rates for four different ICP-RIE parameter combinations. The most stable and plasma-invariable are listed first.

Gases (and their flow)	Temperature	Chamber pressure	ICP power	CCP	DC bias
SF_6 (30 sccm)	-120 °C	10 mTorr	1000 W	20 W	0 V
Ar (25 sccm) and CHF_3 (25 sccm)	-120 °C	10 mTorr	0 W	150 W	395 V
SF_6 (30 sccm)	7 °C	10 mTorr	1000 W	10 W	0 V
SF_6 (30 sccm)	7 °C	10 mTorr	1000 W	20 W	0 V
Gases (and their flow)	**Etch time**	**Etched SiO_2 thickness**	**Etch rate**	**Comment**	
SF_6 (30 sccm)	60 sec	16 nm	0.27 $\frac{nm}{s}$	Most stable	
Ar (25 sccm) and CHF_3 (25 sccm)	28 sec	226 nm	8 $\frac{nm}{s}$	Quite fast	
SF_6 (30 sccm)	20 min	0 nm	0 $\frac{nm}{s}$	Some instability	
SF_6 (30 sccm)	NA	NA	NA	Unstable plasma	

120 °C). The cryogenic stage is cooled down to the set temperature by LN_2. Next, the reaction chamber is evacuated, purged with N2, and pumped to a set pressure of $\sim 10^{-6}$ Torr three times.

3. The process gas (SF_6) is brought into the chamber and its flow value is stabilized. At the same time, the chamber pressure is adjusted to the set value of 10 mTorr.

4. ICP power and constant current power (CCP) are turned on, resulting in plasma and DC bias voltage.

5. Desorbed reaction products will diffuse away from the substrate surface and be pumped out of the reaction chamber.

It is also worth mentioning that if the chamber was last used with other gases than SF_6, one should conduct a conditioning run through of the process. This means running through the entire process without inserting the sample into the chamber. In this way one will make sure that the process is working and the plasma has a nice glow. Sometimes one might not even get the plasma ignited. In these cases one could try a conditioning step without any CCP or ICP power. In this way the chamber will become a little more adjusted to the gases of one's reaction. After this one should run another short run through without inserting the sample, to ensure a nice plasma glow.

After having tested the etch rate of a few parameter combinations (see table 3.5), I found that the most stable and plasma-invariable parameters were to use SF_6 gas with a flow of 30 sccm, temperature of -120 °C, a chamber pressure of 10 mTorr, ICP power of 1000 W, CCP of 20 W. These parameters were used during ICP-RIE etching hereafter.

Table 3.6: Piranha etch solution ratios and strengths. This table show the compound, ratios, initial strength of compound and strength of compounds in the finished solution for the piranha etch solution used to clean the sample.

Compound formula	Mixture ratio	Vol% of compound	Vol% of final solution	My mixture volumes
H_2SO_4	3	95-97 vol%	72.0 vol%[1]	45 mL
H_2O_2	1	30 vol%	7.5 vol%	15mL
H_2O	0	NA	20.5 vol%[1]	0 mL

3.7 Stripping off the rest of the Al layer by wet etching

After the anisotropic dry etching with ICP-RIE, the rest of the Al hard mask was removed. This was done in a similar manner as described in section 3.5, with the etch solution listed in table 3.4. The samples were etched for 45 second, which is 150 % of the time it took to remove a similar 50 nm Al thin film. The extra time is added to ensure that all of the Al is removed.

3.8 Etching the last part of the SiO_2 layer in the pattern of holes with a HF wet etch solution

Before this next step of HF wet etching, it extremely important to have a clean sample. The samples were therefore extensively cleaned by the following steps:

1. Hot acetone bath of 65 °C for 2 hours.
2. Another acetone bath for 20 minutes in ultrasonic (US) bath. This time at room temperature.
3. IPA bath for 1 minute in US bath at room temperature.
4. DI water bath for 10 minutes in US bath at room temperature.
5. Plasma ashing for 2 minutes at 50 % oxygen pressure and power of 90 W.
6. Etching in piranha solution for 10 minutes at 125 °C. The mixture ratios and strength of the various compounds and the final solution can be found in table 3.6[1].
7. Cleansing in DI bath under running DI water for 10 minutes.

After these cleansing steps were done, I could proceed the HF wet etching.

It is important that the patterned holes are completely oxide free before MBE growth is

[1] The final solution vol% is calculated based on the assumption that the strength of the added H_2SO_4 is 96 vol%.

done. This is done by HF wet etching, as it is very SiO_2 selective in its etching and does not etch the silicon. At this point the holes are believed to look similar to what can been seen in figure 3.8, with a thin SiO_2 layer at the bottom of the holes.

Figure 3.8: Illustration of a thin SiO_2 layer at the bottom of the patterned holes. After the dry etching, the patterned holes are likely to have a thin SiO_2 layer at the bottom, covering the Si(111) substrate. This layer is important to remove in order to have NW growth on the underlying silicon.

This thin layer will be removed by HF wet etching. The wet etching is isotropic and will etch in all directions in equal amounts. This etching will therefore widen the holes, but hopefully not too much. The result is dependent on the etching time. The etching time should be just enough to etch through the SiO_2 layer at the bottom. Too short etch time will result in it not being possible to grow NWs in the holes. Too long etch time will widen the holes too much. The desired profile after the HF wet etching can be seen in figure 3.9.

Figure 3.9: The desired profile of the pattern of holes after HF wet etching. In this figure the etching time is just right. The etching has just etched through the entire initial width of the holes, but no excess widening has occured.

Immediately before the HF wet etching, the samples were plasma ashed again. This time for 12 seconds in 30 % oxygen pressure and power of 50 W. The sample were then wet etched in a 1 % HF solution for 30 seconds and then immediately put in a IPA bath, where they were kept until the MBE growth to avoid oxidation of the newly exposed Si(111) at the bottom of the holes.

3.9 Growing nanowires in the holes by MBE

The MBE GaAsSb NW growth was done by one of our research group's PhD Candidates: Dingding Ren. The NWs was grown in the Varian Gen II Modular MBE system at NTNU. The parameters Dingding used for the growth were:

- Before growth was started, the samples was annealed at 700 °C for 5 minutes.
- Substrate temperature of 625 °C.
- Ga pre-deposited for 45 seconds at Ga flux equal to what gives 0.7 $\frac{\mathrm{ML}}{\mathrm{s}}$ of GaAs thin film growth on GaAs (100).
- GaAsSb NW growth for 20 minutes, with Ga flux equal to what gives 0.7 $\frac{\mathrm{ML}}{\mathrm{s}}$ of GaAs thin film growth on GaAs (100), As_2 beam equivalent pressure (BEP) of 2.5 $\times 10^{-6}$ Torr and Sb_2 beam equivalent pressure (BEP) of 4.0 $\times 10^{-7}$ Torr.
- After growth was finished, the CAR temperature was ramped down to a temperature of 100 °C.

One of the NWs obtained after these nine major steps can be seen in figure 3.10.

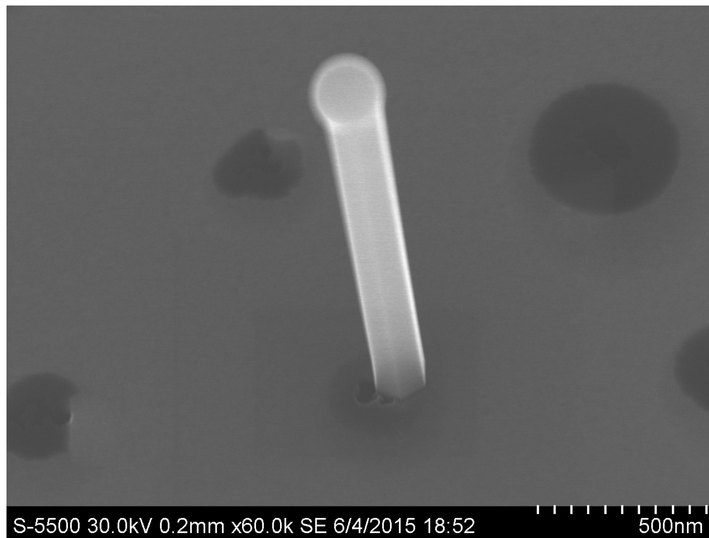

Figure 3.10: One of the NWs obtained after the nine major experimental steps were conducted. In this figure one might see a small darker hole where the NW appears inside a larger more grey hole. It is believed that this is due to underetching in the dry etching step, so that the layer that covers most of the greater whole is SiO_2. In the middle of the image a GaAsSb NW can been seen. It has grown up from the underlying substrate and up through the hole.

Chapter 4

Results and discussion

4.1 Dry etching patterning with electron resist as mask

The goal of this master's thesis was to establish an excellent way of making small sized, flat holes in a SiO_2 layer on top of a Si(111) substrate with a narrow size distribution. Some of the problems with previous techniques have been too wide holes and very uncontrolled size distribution. The techniques that have been tried out before includes simply patterning of the oxide layer with PMMA and then directly transferring the pattern to the oxide layer through HF wet etching. Some of the problems with this technique are illustrated in figure 4.1.

Figure 4.1: Illustration of the HF etch profile of a previously tried out etching technique. Here the problems with HF wet etching directly on the PMMA covered SiO_2 layer on Si(111) are illustrated. As seen in the illustration, the etch profile gets very isotropic as the HF seems to get in between the PMMA and SiO_2 interface during the etching. This results in very uncontrolled hole sizes on the SiO_2 and Si(111) interface. A small difference in etch rate can result in large differences in the SiO_2-Si(111) interface holes, as illustrated by the black lines. The black lines demonstrate the length of the diameter of the SiO_2-Si(111) interface of the different holes.

As seen in figure 4.1, it is very difficult to control the size and size distribution when using this technique. In an attempt to solve these problems, anisotropic dry etching by ICP-RIE was suggested as a middle step between PMMA patterning and HF wet etching. This was supposed to solve the problem in the same manner as described in figures 3.8 and 3.9. However, the selectivity was tested and found to be extremely poor. As explained in section 2.5 (equation 2.5), the selectivity would here be defined as

Table 4.1: Etch rates and selectivity of PMMA and SiO_2. This table shows the data used to calculate etch rates and selectivity for PMMA and SiO_2.

Sample name	**Initial SiO_2 thickness**	**Initial PMMA thickness**	**Final SiO_2 thickness**	**Final PMMA thickness**
U4	307.3 nm	76 nm	234.5 nm	0 nm
U6	307.6 nm	NA	171.0 nm	NA
Sample name	**Etched SiO_2 thickness**	**Etched PMMA thickness**	**Etch time**	**SiO_2 etch rate**
U4	72.8 nm	76 nm	48 sec	NA
U6	136.6 nm	NA	48 sec	2.85 $\frac{\text{nm}}{\text{s}}$

$$S = \frac{\text{Etch rate of material to be patterned}}{\text{Etch rate of mask material}} = \frac{\text{SiO}_2\text{ etch rate}}{\text{PMMA etch rate}} \tag{4.1}$$

The selectivity was found by etching two samples of SiO_2 on top of a Si substrate where one of them was covered with PMMA (sample U4). The samples were etched for 50 seconds, but as it takes a few seconds for the plasma to stabilize, 48 seconds of effective etching were used for the calculation. The thicknesses of SiO_2 layers and the PMMA layer were measured be a F20 reflectometer from Filmetrics before etching and can be found in table 4.1. In this table we see that the etch rate of SiO_2, based on calculation from sample U6, is 2.85 $\frac{\text{nm}}{\text{s}}$. The etch rate of PMMA can be found from sample U4 when using the SiO_2 etch rate from sample U6 as a variable in the following manner:

$$r_{\text{PMMA}_{\text{U4}}} = \frac{d_{\text{PMMA}}}{t_{\text{total}} - \frac{d_{\text{SiO}_{2\text{U4}}}}{r_{\text{SiO}_{2\text{U6}}}}} = \frac{76\text{ nm}}{48\text{ sec} - \frac{72.8\text{ nm}}{2.85\ \frac{\text{nm}}{\text{s}}}} = \frac{76\text{ nm}}{22.4\text{ s}} = 3.39\ \frac{\text{nm}}{\text{s}} \tag{4.2}$$

Thus, the selectivity can be calculated using equation 4.1.

$$S = \frac{\text{SiO}_2\text{ etch rate}}{\text{PMMA etch rate}} = \frac{2.85\ \frac{\text{nm}}{\text{s}}}{3.39\ \frac{\text{nm}}{\text{s}}} = 0.84 \tag{4.3}$$

The selectivity should be as high as possible to ensure that the holes are well etched while the PMMA mask is kept as untouched as possible. As we see here, the selectivity is even less than one, meaning that the mask will be etched away faster than the material to be etched. This is not good, and a better way had to be found. Using PMMA as a mask was still tried out, to see if it would work to use an electron resist as a mask. The results can be seen in figures 4.2, 4.3 and 4.4, and are somewhat promising.

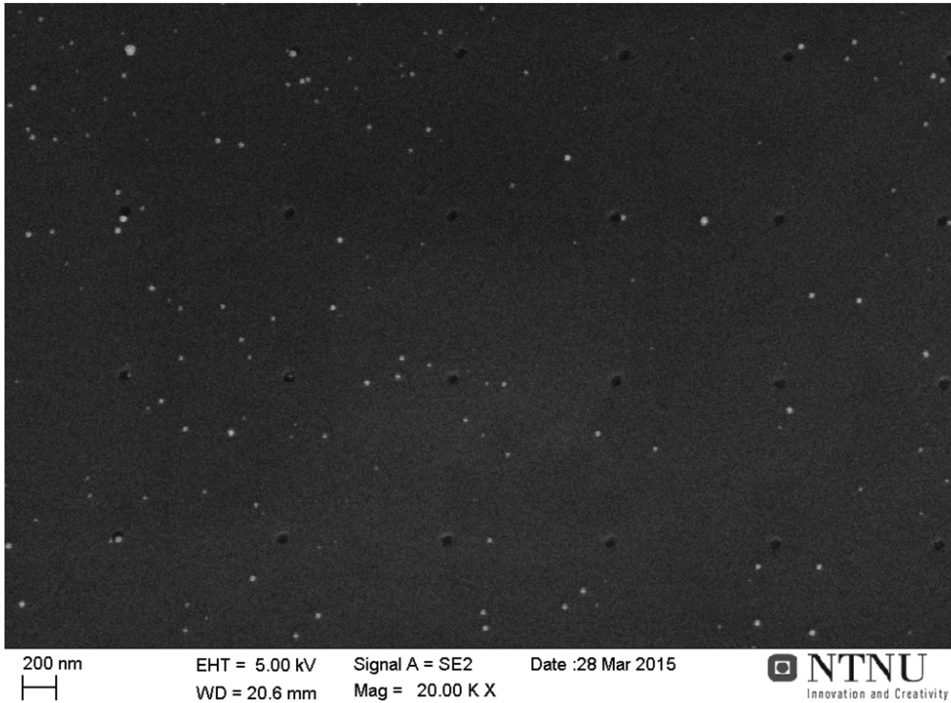

Figure 4.2: SEM image of the pattern of holes in SiO_2 etched by ICP-RIE with a PMMA mask (sample U23). As the PMMA mask had low selectivity, these could only be etched for a limited amount of time and are not very deep (see figures 4.3 and 4.4). The holes have a narrow hole size distribution around 75 nm in diameter.

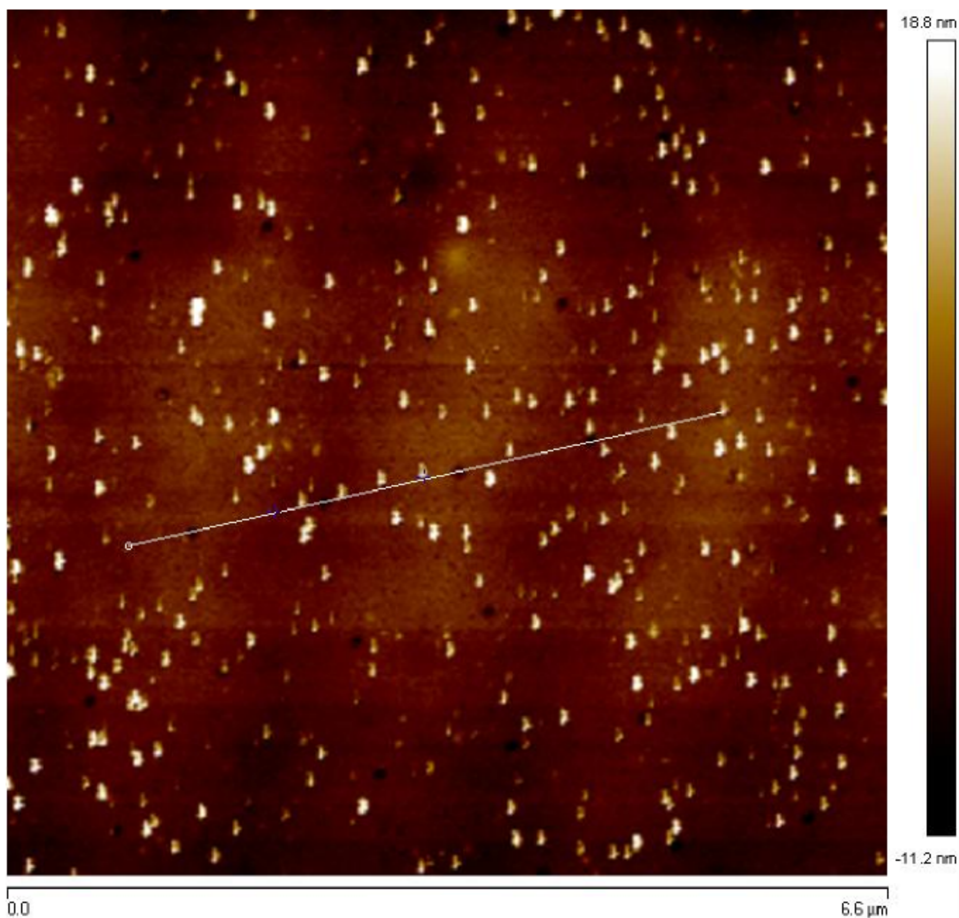

Figure 4.3: AFM image of the pattern of holes in SiO_2 etched by ICP-RIE with a PMMA mask (sample U23). Here, the colors in the image are plotted as a function of height measured by the AFM tip (conversion bar can be seen in the image). The white stripe's height is plotted in figure 4.4.

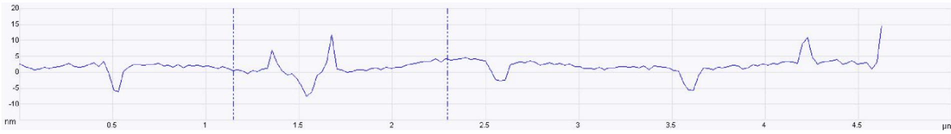

Figure 4.4: AFM profile graph of pattern of holes in SiO_2 etched by ICP-RIE with a PMMA mask (sample U23). The height profile of the white stripe shown in figure 4.3 is shown here. It clearly shows the profile of the first four holes, which seem to have a depth of 5-10 nm. However, they could be deeper, as the AFM tip might be obstructed from reaching the bottom of the holes and thereby creating steep sample artifacts in the image as seen in figure 2.30.

Closer inspection of figures 4.2, 4.3 and 4.4 shows that the pattern of holes all seem fairly similar with a narrow size distribution around 75 nm in diameter. However, the holes are quite shallow, as can be seen from figure 4.4. This is because they were only etched for a short amount of time ($\sim$ 20 seconds), as the PMMA mask would quickly etch away in the plasma due to its high etch rate. However, the holes might be deeper if they are subject to AFM imaging artifacts similar to the one seen in figure 2.30b (section 2.9.2). However, this is still promising results, as it shows the possibility for using electron resists as a direct mask to produce patterned holes with anisotropic dry etching. Other electron resists should be sought out and tested for their selectivity. Particularly, an electron resist named CSAR62 should be investigated, as it has shown very promising selectivity for plasma etching [48]. The research group "Oxide electronics group" at NTNU are currently using this electron resist for their EBL patterning. Another interesting resist which has shown promising results with regard to its plasma dry etching rate, is ZEP 550A, as S. J. Gibson *et al.* have documented [49].

4.2 Dry etching patterning with aluminium as hard mask

A solution to the low selectivity, was to replace the PMMA mask with an Al hard mask, as explained in the experimental chapter (chapter 3). The selectivity of the high quality thermal SiO_2 to the Al was also tested. 16 nm of high quality thermal SiO_2 was etched away in 58 seconds, while the Al hard mask of 50 nm was still not etched away after 30 minutes. This gives us a selectivity of minimum 9.9, which is more than sufficient to securely transfer the pattern. However, there is also a downside with this technique. When one introduces a second pattern transfer step like this, there is also a second step where the pattern transfer may be mismatched. Mismatching of several pattern transfer steps may add onto each other, resulting in an extra distorted pattern transfer. This was also what happened, as one can see in figures 4.5, 4.6, 4.7 and 4.8.

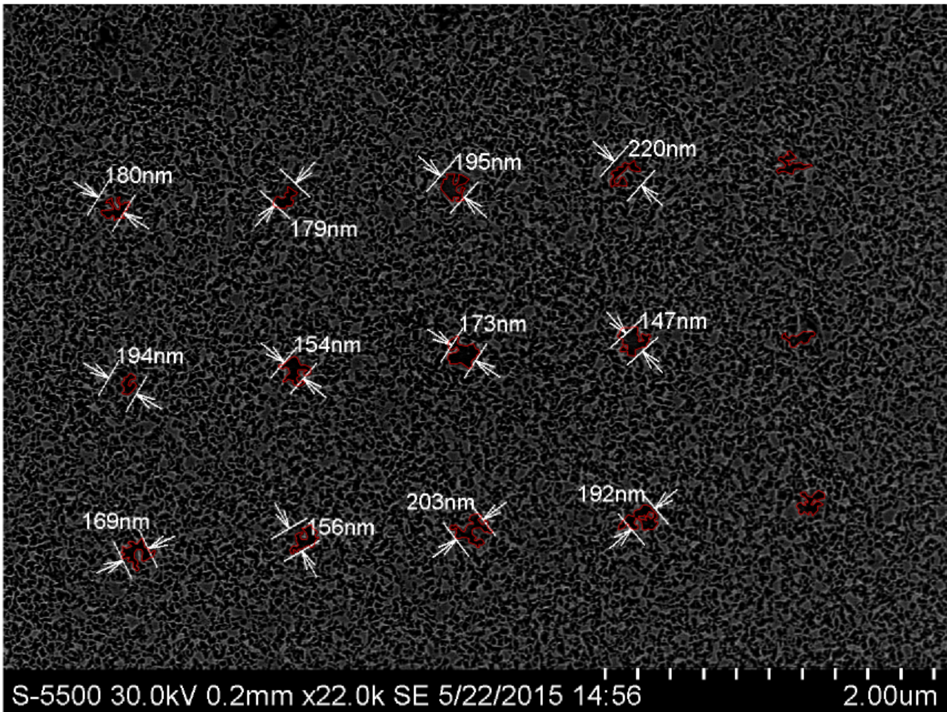

Figure 4.5: SEM image of the pattern of holes transferred from the PMMA mask to the Al hard mask by etching in Al etch solution. The contours of the etched Al holes are highlighted in red, which makes it easy to see that the pattern is not perfectly tranferred. Rather than smooth circular holes, the holes have odd shapes, with parts where all the Al is etched through, and other part where it is not completely etched through. The initial pattern is made by one-shot exposure with 1 ms dwell time (sample U44).

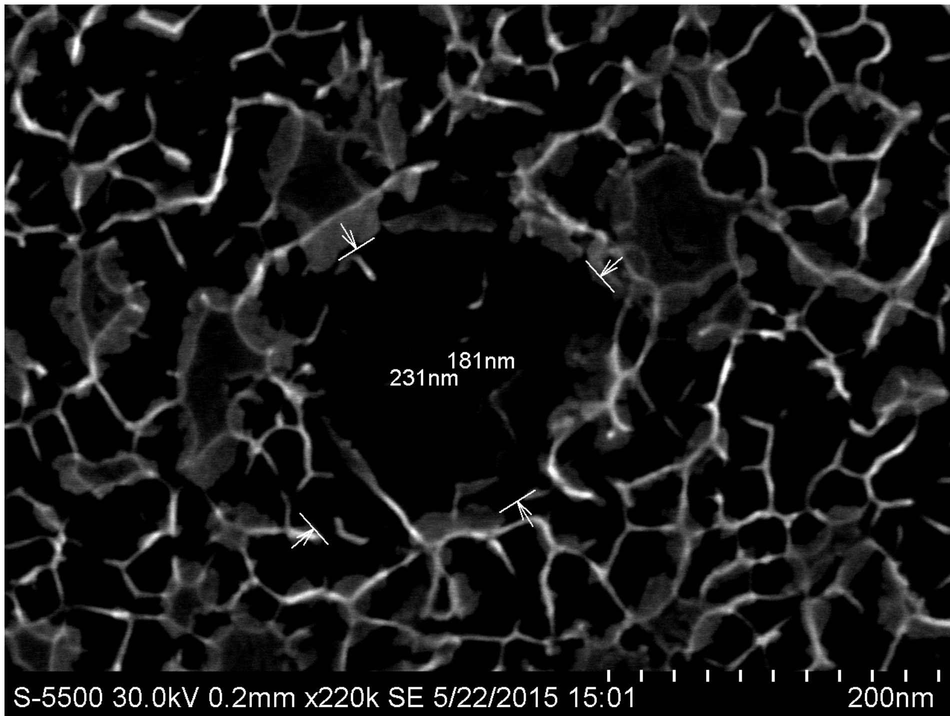

Figure 4.6: Close-up SEM image of the pattern of holes transferred from the PMMA mask to the Al hard mask by etching in Al etch solution. Here it is easier to see how the holes in the Al hard mask are not completely etched through. The initial pattern is made by one-shot exposure with 1 ms dwell time (sample U44).

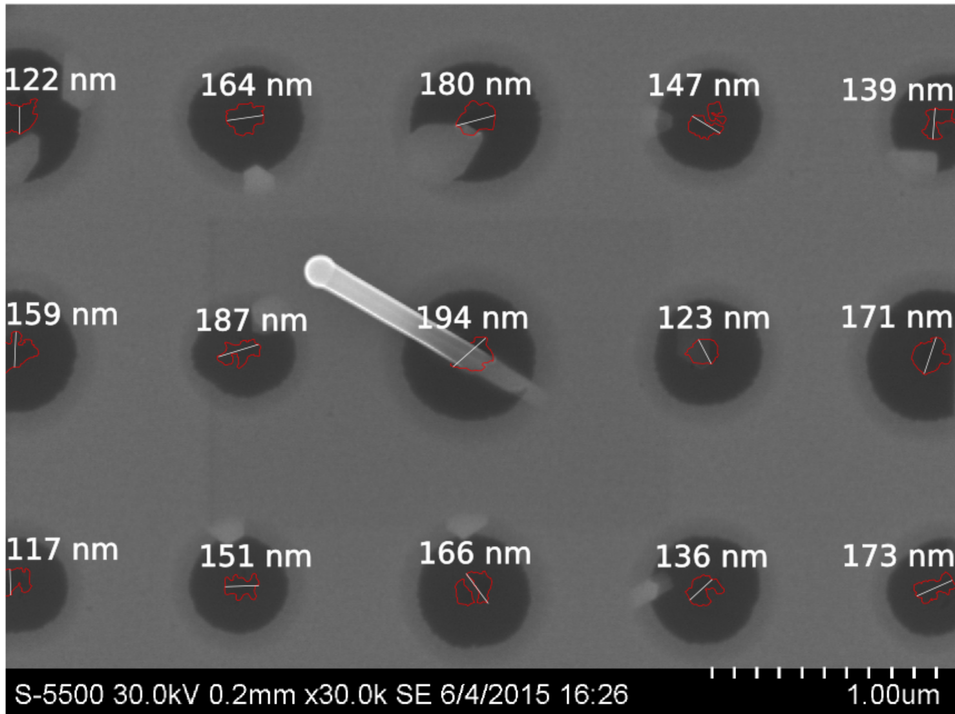

Figure 4.7: SEM image of the pattern of holes transferred from the Al hard mask to the SiO_2 layer by ICP-RIE. The Al has been removed since the ICP-RIE. The contours of the etched out holes in the SiO_2 layer are highlighted in red. Because the pattern transfer to the Al hard mask was not satisfactory, the same defects are transferred to the SiO_2 layer, and the holes achieve odd shapes. The bigger, darker areas around the holes are believed to be a result of heavy undercut from the ICP-RIE (as seen in figure 4.11). In the middle of the image, a GaAsSb NW can be seen. It has grown up from the underlying substrate and up through the hole. The pattern is made by one-shot exposure with 1 ms dwell time (sample U44).

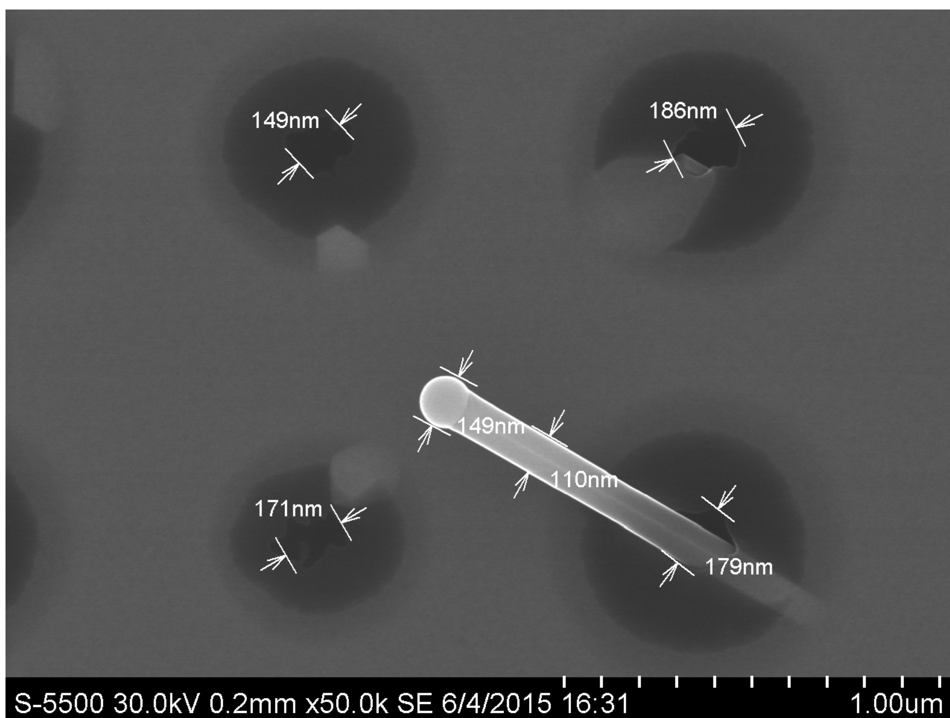

Figure 4.8: Close-up SEM image of the pattern of holes transferred from the Al hard mask to the SiO_2 layer by ICP-RIE. This is a close-up image of figure 4.7. Here it easier to spot the odd-shaped holes in the midlle of the dark, round spots. The odd-shaped holes are believed to be the actual hole in the SiO_2 layer, while the dark, round disks stem from substantial undercutting of the underlying Si(111) substrate, resulting in a so-called loafbread profile, with a see-through thin SiO_2 layer on top.

In figures 4.5 and 4.6 one can see that holes in the Al layer are not perfectly etched through. The shapes of the holes seem quite random. The reason for this might well be that the Al layer forms grains as it is sputtered onto the SiO_2 substrate. These grains probably have a very wide size distribution. The odd shapes seen, are thought to be the contours of the remnants of the different Al grains. A solution to this problem might be to increase the Al etch time to secure that all the grain remnants are gone. This was also tested, and in figure 3.7 one can see the effect of increasing the Al etch time from 150 % to 200 % (from 45 sec to 60 sec). When the holes are etched with etch time of 200 % the holes seem more etched through with less Al features in them. However, it was found that the 905 PMMA A2 resist could not withstand the extra time in the Al etch solution, and a significant overall thinning of the Al layer was observed. This resulted in a poor pattern transfer to the SiO_2 layer. It is believed that in the subsequent ICP-RIE etching of the sample with increased etch time (sample U45), most of the 40 nm thick SiO_2 layer was removed as NW growth was observed all over the sample (see figure 4.9).

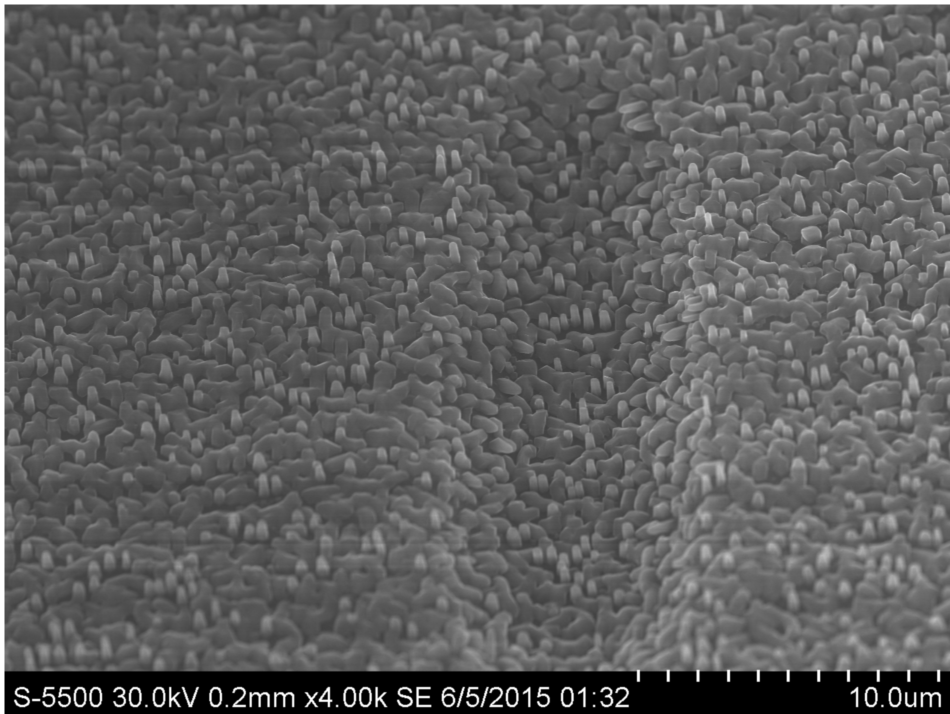

Figure 4.9: Close-up tilted SEM image of NWs at sample with increased Al etch time. In this image one can see that after ICP-RIE dry etching, HF wet etching and MBE NW growth, the NWs where found growing all over the sample. This indicates that the 40 nm thick SiO_2 layer was completely removed during the dry etching due to significant thinning of the Al hard mask layer from the increased etch time of 200 % in the Al etch pattern transfer step. The sample (sample U45) is tilted at 30°. The surface seen in this image is quite rough. The rough features seen are believed to be GaAsSb crystals from the MBE growth that are forming everywhere, almost as a layer, as the SiO_2 layer is likely to be completely removed, and thus exposing the Si(111) substrate below.

The result of using these oddly shaped holes in the Al layer, is that the holes in the 40 nm thick SiO_2 layer will take on the same shapes. In figures 4.7 and 4.8 one can see that the pattern transfer resulted in oddly shaped holes in the SiO_2 layer. In figure 4.7 one can also see large dark regions around the hole openings. The dark regions are believed to stem from significant undercut of the Si(111) substrate due to bending of the beam as a result from electron accumulation on the edges of the holes (see section 2.5 and figure 4.10) combined with too long etch time. As silicon is known to have higher selectivity than SiO_2 for fluoride based plasma etching techniques, the undercut will develop rapidly once the plasma etches through the SiO_2 layer. This is the reason we wanted to not etch completely through the SiO_2 layer, but keep a thin film of it at the bottom of the holes (figure 3.8) to be etched away with HF wet etching. The etch time of the ICP-RIE dry etching was set to 150 % of the time it would take to etch through an equally thick SiO_2 thin film. The reason for the prolonged etch time is to account for the loading effect that

occurs in deep trenches and holes where the etch rate is reduced due to the limitation of the circulation of the gas species in small-scaled features. As the holes are nanoscaled in two direction this further enhances the loading effect, compared to nanoscaled trenches. Waste products from the etching inside the holes must diffuse out of the holes, and at the same time new reactive species must enter. When comparing to flat surface etching, as thin film etching is, it is clear that the etch time must be increased to obtain the desired depth. However, 150 % was likely too much for this particular etch procedure (figures 4.5 and 4.6). The overetching may have resulted in profile similar to the one seen in figure 4.11 and therefore resulting in NWs that grow out of the holes at a sharp angle.

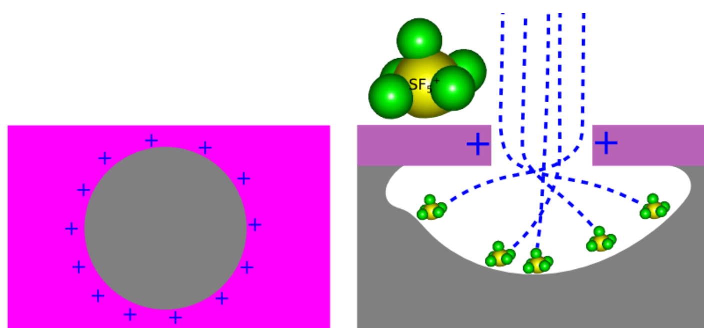

Figure 4.10: Undercut of SiO_2 layer because charge build-up bends the ions. Charge build-up on the edges of the holes might bend the path of the positively charged SF_5^+ ions, resulting in undercut of the thermal SiO_2 layer.

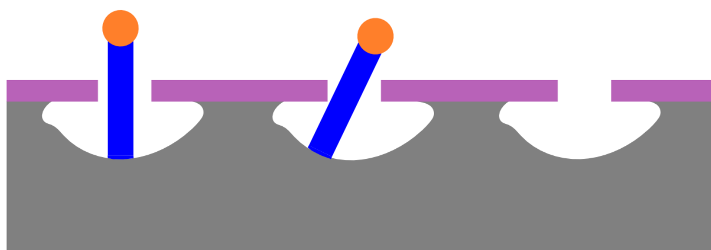

Figure 4.11: Uneven profiles might lead to NWs growing at an angle. When the bottom of the holes is not flat, the NWs might end up growing and exiting the SiO_2 layer at an angle. This can be seen in the SEM image of figure 4.8.

Al hard mask layer thickness

The size distribution of the holes made by etching of the Al with a patterned PMMA mask was also investigated as a function of Al layer thickness. Initially an Al hard mask of 200 nm thickness was used. It was observed very large hole size distribution with this Al layer thickness, as can be seen in figure 4.12a. Based on figure 4.12a, an average hole size of 182 nm and a standard deviation of 58 nm (32 %) was found. It was thought that limit-

ing the etching time of the Al layer would decrease the large variance in size distribution. Therefore, the thickness of the Al layer was reduced to 50 nm, thus reducing the etch time needed to etch through the layer. This sample is imaged in figure 4.12b. An average size of 196 nm and a standard deviation of 37 nm (19 %) was found based on this image. However, the etched holes in the 50 nm thick layer show that there are Al grains remnants left in the holes due to the short etch time. This leaves the holes more irregular than the ones etched in the 200 nm thick Al layer. This irregularity is not favorable and countermeasures should be made to avoid it.

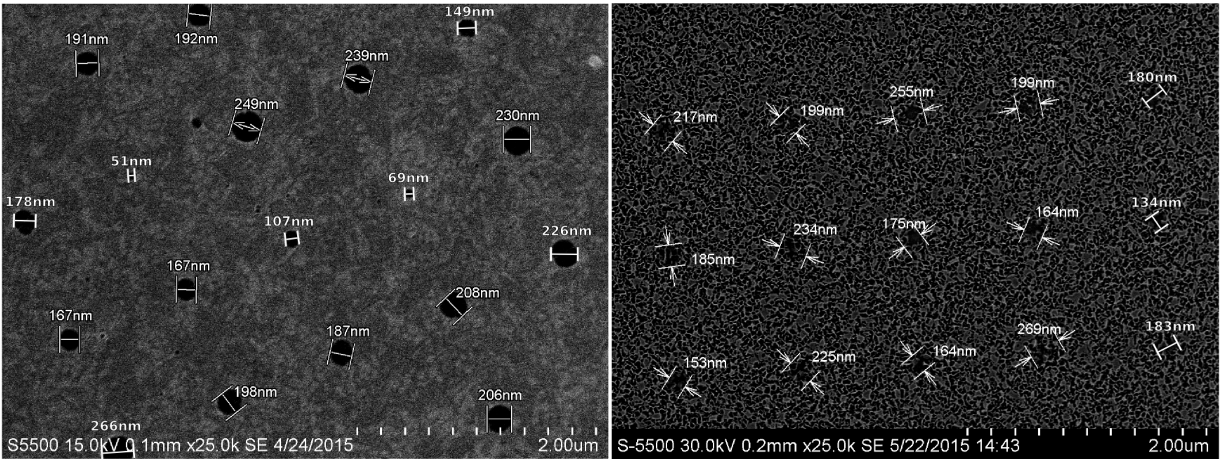

(a) Sample U36 with a 200 nm thick Al layer on Si(100).

(b) Sample U44 with a 50 nm thick Al layer on a 40 nm thick thermal SiO_2 layer on Si(111).

Figure 4.12: Size distribution of the holes on the Al layers. In (**a**) one can see sample U36, that is EBL patterned with one-shot exposure with 1.0 ms dwell time. The pattern has been transferred to the Al thin film by etching in the Al etch solution (table 3.4) for 156 seconds and the resist has then been removed. The average hole size is 182 nm, with a standard deviation of 58 nm (32 %). In (**b**) one can see sample U44, that is EBL patterned with one-shot exposure with 0.75 ms dwell time. The pattern has been transferred to the Al thin film by etching in the Al etch solution for 45 seconds and the resist has then been removed. The average hole size is 196 nm, with a standard deviation of 37 nm (19 %).

It is believed that a thinner Al layer will yield holes with a narrower hole size distribution as the etching time is reduced. However, it is important that the Al layer thickness is sufficiently thick so that the layer is not etched through during the ICP-RIE etching. A 50 nm thick Al layer has been found to withstand 30 minutes of ICP-RIE etching with the etching parameters used in this study, which is more than sufficient. Therefore, one might try with even thinner Al layers as they will probably withstand the plasma dry etching, which will be less than 5 minutes.

If thinner Al layers are tried out, the relative Al wet etching time should be increased. As can be seen in figure 4.5, the Al layer seem to not be thoroughly etched through. By keeping the etch time constant, at e.g. 45 seconds, while the Al layer is made thinner, the hole profile might be more even as the Al grains remnants should be more quickly removed. This should lead to a better Al hole profile. The PMMA layer has already been proven to withstand 45 seconds in the Al etch solution.

4.3 Effect of EBL parameters

Most of the patterning done by EBL in this study was done by the one-shot method (section 2.3.3). One problem with this method might be that the hole are not evenly exposed. The center of the hole will receive more exposure as the beam is most concentrated in the middle, and this might have resulted in a PMMA profile similar to the one seen in figure 4.13. This could result in a similar profile for the holes in the Al layer after the hard mask wet etching step (step 5). One way to reduce this effect could be through other EBL patterning modes. Area exposure mode and especially circular exposure mode could prove useful to improve the PMMA profile after EBL exposure, however, at a small cost of prolonged exposure times. As we have seen in section 2.3.3, the exposure time will have a large increase in the relative value, however, in absolute value it is just a matter of ~ 2 minutes.

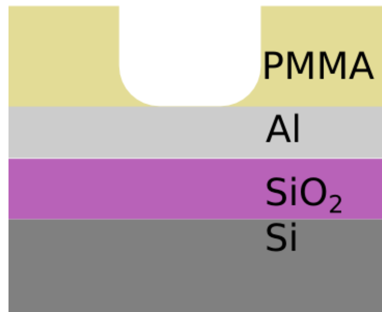

Figure 4.13: Illustration of the PMMA patterning profile. Due to the beam being more concentrated in its center, the PMMA profile might get an unwanted profile when the one-shot exposure mode is used.

4.4 Effect of ICP-RIE etching

The ICP-RIE dry etching step is crucial when it comes to developing holes in the SiO_2 layer with a high aspect ratio and good anisotropy. From the image in figure 4.8 one can see the odd shaped holes in the thin SiO_2 layer. Thee holes seem to have the same odd shapes as the holes that were seen in the Al layer before ICP-RIE dry etching (figure 4.5). This may indicate that the pattern transfer from the Al layer to the SiO_2 layer by ICP-RIE went quite well. The odd shapes would not have persisted if the dry etching had a lot of

isotropic and lateral etching of the SiO_2 layer. Further testing should be conducted with SF_6 as the reactive species, but with increased focus on not etching completely through the SiO_2 layer.

4.4.1 Choosing the material to be patterned and the material to be the hard mask

It is not necessarily SiO_2 that is the best material to pattern the Si substrate with. Other patterning layers should be sought out, such as Si_3N_4. Patterned dry etching with use of a hard mask has already been done and published for Si_3N_4 (figure 4.14) [50]. In this study Al_2O_3 was used as a hard mask. The etching parameters can be found in table 4.2.

However, if Al_2O_3 is to be used as a hard mask, it is very important to be able to remove all of this hard mask before the sample are put inside the MBE chamber for growth. This is because the NWs will easily nucleated and start forming crystals on the Al_2O_3 surface. An advantage of not using Al as the hard mask, is that one does not have to deal with the random grain sizes that form when Al is deposited. Therefore, one should be able to achieve smoother holes in the hard mask (as opposed to the holes seen in figure 4.5).

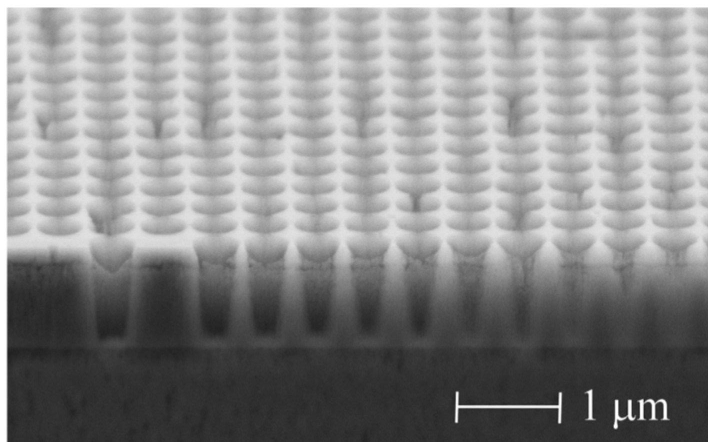

Figure 4.14: Etching profile of low pressure chemical vapor deposition (LPCVD) Si_3N_4. Here, patterned Al_2O_3 was used as a hard mask. Etching parameters can be found in table 4.2. The image is taken from Nabar *et al.* [50]. The width of the patterned holes seen in this image is 400 nm and the depth is 1 μm. The selectivity of Si_3N_4 to Al_2O_3 was found to be 24.75:1.

Table 4.2: ICP-RIE parameter for etching of Si_3N_4. This table shows the parameters used by Nabar *et al.* [50] to etch Si_3N_4 with a Al_2O_3 hard mask (see figure 4.14).

Etched material	LPCVD Si_3N_4
Hard mask	Al_2O_3
Gasses	CHF_3 and He
ICP power	4500 W
RF power	35 W
Chamber pressure	11 mTorr

Chapter 5

Conclusion and future work

In this master's thesis it has been shown that using ICP-RIE for etching more anisotropic and equal holes for the growth of NWs shows promising results. It is a technique that efficiently deals with the problem of too isotropic holes when wet etching has been used earlier. With the use of a masking layer, one can etch holes in a SiO_2 layer with a narrow size distribution and little widening of the holes. It has been shown that using an electron resist directly as the masking material is possible, but that the electron resist called 950 PMMA A2 has too high etch rate in the plasma for it to be a viable candidate. Hard mask layers, such as Al, can also be an option. However, results indicate that if Al hard mask is used, the layer thickness should be kept as thin as possible. Al has a very low etch rate in the plasma dry etching and very thin layers should be compatible with its use as a hard mask.

Results have also highlighted the importance of not etching through the entire SiO_2 layer during ICP-RIE, and the last bit of the SiO_2 layer should be etched away with a HF wet etch solution. An increased ICP-RIE etch time of 150 %, due to reduced etch rate in small scale features, was found to have etched through the SiO_2 layer, and this parameter should be reduced.

5.1 Future work

Future work would first and foremost be to conduct similar experiments where other electron resists are used as a mask. Both the resists CSAR 62 [48] and ZEP 550A [49] should be looked into. Hopefully, one or more will have a low enough selectivity compared to the SiO_2 in the ICP-RIE plasma to be able to be used as the sole mask for the process. Testing of the amount of extra etch time needed for nanoscaled features compared to thin films on SiO_2 should also be done. Exposing of the electron resist could preferentially be done with circular exposure mode and be compared with area exposure mode and one-shot exposure mode.

Bibliography

[1] Å. S. ueland, *Modelling and characterisation of self-catalysed GaAs nanowire growth by use of molecular beam epitaxy*. 2014. Student project at Department of Electronics and Telecommunications, the Norwegian University of Science and Technology.

[2] E. Ertekin, P. A. Greaney, C. D. Chrzan and T. D. Sands, *Equilibrium limits of coherency in strained nanowire heterostructures*. 2005. J. Appl. Phys. **97**, p. 114325.

[3] S. Raychaudhuri and E. T. Yu, *Critical dimensions in coherently strained coaxial nanowire heterostructures*. 2006. J. Appl. Phys. **99**, p. 114308.

[4] F. Glas, *Critical dimensions for the plastic relaxation of strained axial heterostructures in free-standing nanowires*. 2006. Phys. Rev. B **74**, p. 121302.

[5] `https://www.crystec.com/tridepe.htm`
(Content accessed 13.06.15)

[6] J. Tavares, E. J. Swanson ans S. Coulombe, *Plasma Synthesis of Coated Metal Nanoparticles with Surface Properties Tailored for Dispersion*. 2008. Plasma Processes and Polymers **5**, p. 759.

[7] `http://telemark.com/electron_beam_sources/arc_suppression.php?cat=1&id=Arc+Suppression+Sources`
(Content accessed 15.06.2015)

[8] J. George, *Preparation of thin films*. 1992. Marcel Dekker, Inc., New York, pp. 9-13.

[9] S. V. Kesapragada *et al.*, *Nanospring pressure sensors grown by glancing angle deposition*. 2006. Nano letters **6.4**, pp. 854-857.

[10] KTH The Royal Institute of Technology Department of Applied Physics. Raith 150 e-beam lithography software.

[11] M. A. McCord and M. J. Rooks, *Electron beam lithography* in P. Rai-Choudhury, editor, *Handbook of Microlithography, Micromachining, and Microfabrication, volume 1*. 1997. SPIE Press.

[12] S. Sandell, *Process development for fabrication of GaAs nanowire array solar cell*. 2012.

[13] P. Verdonck, *Plasma Etching*. 2006. V Oficina de Microeletrônica.

[14] J.R. Arthur, *Molecular beam epitaxy*. 2002. Surface Science **500**, pp. 189-217.

[15] D.D.L. Narayana, *Growth and structural characterization of III-V nano wires grown by molecular beam epitaxy*. Doctoral thesis at NTNU, 2010: **190**, pp. 24-26.

[16] K. Oura, V. G. Lifshits, A. A. Saranin, A. V. Zotov and M. Katayama, *Surface Science: An Introduction*. 2001. Springer-Verlag: Berlin, pp. 59–65.

[17] W. Braun, *Applied RHEED: Reflection High-Energy Electron Diffraction During Crystal Growth*. 1999. Springer-Verlag: Berlin, pp. 14–17, 25, 75.

[18] A. M. Munshi, *Epitaxial Growth of Self-Catalyzed GaAs Nanowires by Molecular Beam Epitaxy*. 2014. Doctoral Thesis at NTNU.

[19] R. S. Wagner, W. C. Ellis, *Vapor-liquid-solid mechanism of single crystal growth*. 1964. Appl. Phys. Lett. **4**, p. 89.

[20] Z. H. Wu, X. Y. Mei, D. Kim, M. Blumin and H. E. Ruda, *Growth of Au-catalyzed ordered GaAs nanowire arrays by molecular-beam epitaxy*. 2002. Applied Physics Letters **81**, pp. 5177-5179.

[21] D.L. Dheeraj, H.L. Zhou, A.F. Moses, T.B. Hoang, A.T.J. van Helvoort, B.O. Fimland and H. Weman, *Heterostructured III-V Nanowires with Mixed Crystal Phases Grown by Au-Assisted Molecular Beam Epitaxy* 2010. Nanowires, Paola Prete (Ed.), ISBN: 978-953-7619-79-4, InTech, DOI: 10.5772/39503. Available from: `http://www.intechopen.com/books/nanowires/heterostructured-iii-v-nanowires-with-mixed-crystal-phases-grown-by-au-assisted-molecular-beam-epita`

[22] J. C. Harmand, G. Patriarche, N. Pere-Laperne, M. N. Merat-Combes, L. Travers and F. Glas, *Analysis of vapor-liquid-solid mechanism in Au-assisted GaAs nanowire growth*. 2005. Applied Physics Letters **87**, pp. 203101-203103.

[23] C. Chen, M. C. Plante, C. Fradin and R. R. LaPierre, *Layer-by-layer and step-flow growth mechanisms in GaAsP/GaP nanowire heterostructures*. 2006. Journal of Material Research **21**, pp. 2801-2809.

[24] J. E. Allen, E. R. Hemesath, D. E. Perea, J. L. Lensch-Falk, Z. Y. Li, F. Yin, M. H. Gass, P. Wang, A. L. Bleloch, R. E. Palmer, L. J. Lauhon, *High-resolution detection of Au catalyst atom in Si nanowires*. 2008. Nature Nanotech. **3**, p. 168.

[25] D. E. Perea, J. E. Allen, S. J. May, B. W. Wessels, D. N. Seidman, L. J. Lauhon, *Three-dimensional nanoscale composition mapping of semiconductor nanowires*. 2005. Nano Lett. **6**, p. 181.

[26] M. Bar-Sadan, J. Barthel, H. Shtrikman, L. Houben, *Direct imaging of single Au atoms within GaAs nanowires*. 2012. Nano Lett. **6**, p. 181.

[27] A. Fontuberta i Morral, c. Colombo, G. Abstreiter, J. Arbiol, J. R. Morante, *Nucleation mechanism of gallium-assisted molecular beam epitaxy growth of gallium arsenide nanowires*. 2008. Appl. Phys. Lett. **92**, p. 063112.

[28] Y. Wu and P. Yang, *Direct Observation of Vapor-Liquid-Solid Nanowire Growth*. 2001. Journal of the American Chemical Society **123**, pp. 3165-3166.

[29] A. M. Munshi, D. L. Dheeraj, V. T. Fauske, D. C. Kim, J. Huh, J. F. Reinertsen, L. Ahtapodov, K. D. Lee, B. Heidari, A. T. J. van Helvoort, B. O. Fimland and H. Weman, *Position-Controlled Uniform GaAs Nanowires on Silicon using Nanoimprint Lithography*. 2014. Nano Letters **14**, pp. 960-966.

[30] T. Mårtensson, P. Carlberg, M. Borgström, L. Montelius, W. Seifert and L. Samuelson, *Nanowire arrays defined by nanoimprint lithography*. 2004. Nano Letters **4**, pp. 699-702.

[31] A. Pierret, M. Hocevar, S. L. Diedenhofen, R. E. Algra, E. Vlieg, E. C. Timmering, M. A. Verschuuren, G. W. G. Immink, M. A. Verheijen and E. P. A. M. Bakkers, *Generic nanoimprint process for fabrication af nanowire arrays*. 2010. Nanotechnology **21**, 065305.

[32] A. L. Roest, M. A. Verheijen, O. Wunnicke, S. Serafin, H. Wondergem and E. P. A. M. Bakkers, *Positioned-controlled epitaxial III-V nanowires on silicon*. 2006. Nanotechnology **17**, S271.

[33] T. Mårtensson, M. Borgström, W. Seifert, B. J. Ohlsson and L. Samuelson, *Fabrication of individually seeded nanowire arrays be vapor-liquid-solid growth*. 2003. Nanotechnoogy **14**, p. 1255.

[34] P. Mohan, J. Motohisa and T. Fukui, *Controlled growth of highly uniform, axial/radial direction-defined, individually addressable InP nanowire arrays*. 2005. Nanotechnology **16**, p. 2903.

[35] D. S. Kim, R. Ji, H. J. Fan, F. Bertam, R. Scholz, A. Dadgar, K. Nielsch, A. Krost, J. Christen, U. Gösele and M. Zacharias, *Laser-interference lithography tailored for highly symmetrically arranged ZnO nanowires arrays*. 2006. Small **3**, pp. 76-80.

[36] X. Zhang, Y. Hao, G. Meng and L. Zhang, *Fabrication of highly ordered InSb nanowire arrays by electrodeposition in porous anodic alumina membranes*. 2005. Journal of the Electrochemical Society **152**, pp. C664-C668.

[37] G. I. Goldstein, D. E. Newbury, P. Echlin, D. C. Joy, C. Fiori and E. Lifshin, *Scanning electron microscopy and x-ray microanalysis*. 1981. New York: Plenum Press.

[38] K. Tanaka, A. Mitsushima, Y. Kashima, T. Nakadera and H. Osatake, *Application of an ultrahigh-resolution scanning electron microscope (UHS-T1) to biological specimens*. 1989. Journal of Electron Microscopy Technique Volume **12**, pp. 146-154.
(Content accessed 26.10.14)

[39] K. M. Lang, D. A. Hite, R. W. Simmonds, R. McDermott, D. P. Pappas and J. M. Martinis. *Conducting atomic force microscopy for nanoscale tunnel barrier characterization*. 2004. Review of Scientific Instruments **75**, pp. 2726–2731.

[40] G. Binnig, C. F. Quate and Ch. Gerber, *Atomic Force Microscope*. 1986. Physical Review Letters **56**, pp. 930–933.

[41] Q. Zhong, D. Inniss, K. Kjoller and V. Elings, *Fractured polymer/silica fiber surface studied by tapping mode atomic force microscopy*. 1993. Surface Science Letters **290**, p. 688.

[42] N. A. Geisse, *AFM and Combined Optical Techniques*. 2009. Materials Today **12**, pp. 40–45.

[43] L. Gross, F. Mohn, N. Moll, P. Liljeroth and G. Meyer, *The Chemical Structure of a Molecule Resolved by Atomic Force Microscopy*. 2009. Science **325**, pp. 1110–1114.

[44] F. J. Giessibl, *Advances in atomic force microscopy*. 2003. Reviews of Modern Physics **75**, pp. 949–983.

[45] R. V. Lapshin, *Feature-oriented scanning methodology for probe microscopy and nanotechnology*. 2004. Nanotechnology **15**, pp. 1135–1151.

[46] R. V. Lapshin, *Automatic drift elimination in probe microscope images based on techniques of counter-scanning and topography feature recognition*. 2007. Measurement Science and Technology **18**, pp. 907–927.

[47] V. Y. Yurov and A. N. Klimov, *Scanning tunneling microscope calibration and reconstruction of real image: Drift and slope elimination*. 1994. Review of Scientific Instruments **65**, pp. 1551–1557.

[48] M. Schirmer, B. Büttner, F. Syrowatka, G. Schmidt, T. Köpnick and C. Kaiser, *Chemical Semi-Amplified Positive E-Beam Resist CSAR 62 for Highest Resolution*. 2013. Proc. of SPIE Vol. **8886**, pp. 88860D–1-88860D–7.

[49] S. J. Gibson, J. P. Boulanger and R. R. LaPierre, *Opportunities and pitfalls in patterned self-catalyzed GaAs nanowire growth on silicon*. 2013. Semicond. Sci. Technol. **28**, pp. 105025-105033.

[50] B. P. Nabar, Z. Çelik-Butler, B. H. Dennis and R. E. Billo, *A nanoporous silicon nitride membrane using a two-step lift-off pattern transfer with thermal nanoimprint lithography*. 2012. J. Micromech. Microeng. **22**, pp. 045012-045019.

Chapter 6

Appendix

6.1 ICP-RIE dry etching parameters and their functions

The following steps list, arrange and describes the function of all the necessary procedures of ICP-RIE etching used at our samples.

1. When the sample has been loaded into the reaction chamber, helium (He) flows against the backside of the sample carrier to achieve a set pressure of 10 Torr. This will ensure that the sample is properly cooled, because He is continuously cooled by liquid nitrogen (LN_2). The value of the He flow that is required to achieve the set pressure of 10 Torr will be displayed at the computer screen during this step. Large values (> 10 standard cubic centimeters per minute (SCCM)) indicate that He is leaking into the chamber. At this point one can choose to abort the whole etching process if the leak is substantial enough. Leaking is caused by incomplete sealing between the sample carrier and the wafer clamp above it, and can usually be reduced by repositioning the carrier in the loading arm, so that the wafer perfectly aligns with the wafer clamp.

2. Since our process will take place at -120 °C, the next step is usually cooling of the stage (unless the intrument has just been used at this temperature, and is already at - 120 °C). The cryogenic stage is cooled down to the set temperature by LN_2. Next, the reaction chamber is evacuated, purged with N2, and pumped to a set pressure of $\sim 10^{-6}$ Torr. These steps ensure that any contaminations and moisture that was brought in with the sample are minimized before the process starts. In the software there are tolerance limits that prevent the process from proceeding before the conditions are in accordance with the set parameters.

3. The process gas (SF_6) is brought into the chamber and its flow value is stabilized. At the same time, the chamber pressure is adjusted to the set value of 10 mTorr.

4. ICP power and constant current power (CCP) are turned on, resulting in plasma and DC bias voltage. It is important to observe the plasma luminosity to ensure that both ICP plasma and CCP plasma are ignited. ICP plasma is bright and positioned further up towards the ICP coil, while CCP plasma is dim and positioned closer to the substrate. There are two capacitors for each power generator, that are automatically adjusted from given starting values in order to match the impedance of the power supply with the load. This maximizes the power transfer from the power supply to the plasma. Because the impedance of the plasma

varies with process conditions, the matching values depend on the recipe used. Even though this is normally an automatic process, it might malfunction, causing most of the power to be reflected back to the generator. If this happens, a safety in the software shuts down the process to prevent the generators from overheating. The starting values can be manually adjusted to try to overcome the matching malfunction.

5. The highly reactive, neutral fluorine radicals that are formed in the plasma diffuse from the glow discharge region toward the substrate. At the same time, positive ions (e.g. SF_5^+) generated in the plasma are accelerated toward the substrate by the DC bias.
6. Radicals adsorb onto the SiO_2 substrate and the Al hard mask, and subsequently react with the atoms in these materials to form complexes that are more or less volatile.
7. Accelerated ions collide with surface atoms and adsorbed complexes, and transfer energy that can facilitate several processes leading to increased reaction rate. Firstly, ions can break bonds between surface atoms, forming active sites for the incoming radicals. Secondly, ions can supply the energy needed for covalent bond formation in the adsorbed complexes. Thirdly, ions may facilitate rearrangement of surface atoms to expose binding sites. Finally, ion bombardment will facilitate desorption of the final etch products [13].
8. Desorbed reaction products will diffuse away from the substrate surface and be pumped out of the reaction chamber.